

Learning out-of-time-ordered correlators with classical kernel methods

John Tanner,^{1,*} Jason Pye,^{1,2} and Jingbo Wang^{1,†}

¹*Department of Physics, University of Western Australia, 35 Stirling Hwy, Crawley WA, 6009, Australia*

²*Nordita, Stockholm University and KTH Royal Institute of Technology,*

Hannes Alfvéns väg 12, SE-106 91 Stockholm, Sweden

(Dated: September 3, 2024)

Out-of-Time Ordered Correlators (OTOCs) are widely used to investigate information scrambling in quantum systems. However, directly computing OTOCs with classical computers is often impractical. This is due to the need to simulate the dynamics of quantum many-body systems, which entails exponentially-scaling computational costs with system size. Similarly, exact simulation of the dynamics with a quantum computer (QC) will generally require a fault-tolerant QC, which is currently beyond technological capabilities. Therefore, alternative approaches are needed for computing OTOCs and related quantities. In this study, we explore four parameterised sets of Hamiltonians describing quantum systems of interest in condensed matter physics. For each set, we investigate whether classical kernel methods can accurately learn the XZ-OTOC as well as a particular sum of OTOCs, as functions of the Hamiltonian parameters. We frame the problem as a regression task, generating labelled data via an efficient numerical algorithm that utilises matrix product operators to simulate quantum many-body systems, with up to 40 qubits. Using this data, we train a variety of standard kernel machines and observe that the best kernels consistently achieve a high coefficient of determination (R^2) on the testing sets, typically between 0.9 and 0.99, and almost always exceeding 0.8. This demonstrates that classical kernels supplied with a moderate amount of training data can be used to closely and efficiently approximate OTOCs and related quantities for a diverse range of quantum many-body systems.

I. INTRODUCTION

In recent years, there have been significant technical advances in quantum computing technologies. From photons, trapped ions and neutral atoms, to nuclear magnetic resonance and superconducting qubits [1–5], these technologies work alongside theoretical research by providing opportunities to investigate a qualitatively rich variety of quantum many-body systems. Access to these experimental platforms has not only led to the emergence of novel ideas and new research directions, but has also facilitated the development of mathematical models and tools for characterising numerous aspects of quantum many-body dynamics. In particular, quantum information scrambling [6] has become an active research topic, which investigates the propagation of local quantum information into non-local degrees of freedom, with the aim of characterising quantum many-body systems.

Initially considered in the context of black holes [7–10], scrambling is now studied in more general many-body systems [6, 11–13], often through the lens of the so-called out-of-time-ordered correlator (OTOC) [14, 15]. The OTOC, which first appeared over 50 years ago [16], is a measure of the non-commutativity of Heisenberg operators separated in time. In quantum field theories, the commutator captures causal relationships between observables at different points in spacetime. Accordingly, the OTOC can be viewed as a measure of whether a local operator can causally influence measurements of another spatially-distant operator after some time. The value of the OTOC thus provides a kind of information-theoretic “light cone,” illustrating how information propagates through a system. The light cone is often sharper than the general Lieb-Robinson bound [17], and can exhibit a range of interesting behaviours. For example, chaotic quantum systems exhibit a linear light cone [18], many-body localised systems exhibit logarithmic light cones [19–22], and other marginal systems exhibit light cones somewhere between linear and logarithmic [23].

OTOCs have also been used in discussions of quantum

* john.tanner@uwa.edu.au

† jingbo.wang@uwa.edu.au

chaos [24–26], including in the study of black holes [27], thermalisation [28, 29], and many-body scarred systems [30]. The early-time exponential growth of the OTOC was initially thought to be a diagnosis of chaos, and was even used to define a quantum analogue of the Lyapunov exponent [31] and the Lyapunov spectrum [32]. However, more recent findings have revealed that the exponential growth of OTOCs is necessary but not sufficient to diagnose chaos in quantum systems [33], suggesting that this connection requires further research. This, together with the significant role that the OTOC plays in studying quantum information scrambling and other intriguing applications [34, 35], provides compelling reasons to undertake detailed investigations of the OTOC.

Classical methods for calculating OTOCs require the simulation of a quantum many-body system, a task which generally involves computational costs that scale exponentially in the size of the system. This makes the implementation of these methods extremely difficult in practice. There are, however, a handful of specific quantum systems for which the OTOC can be determined efficiently with classical methods. This includes exactly solvable cases, such as the Sachdev-Ye-Kitaev model [36, 37], 1-dimensional (1D) quantum Ising spin chain [38], and other integrable systems [39]. Similarly, for 1D systems evolving under local Hamiltonians (such as those considered in this work), tensor network methods can be used to reliably estimate OTOCs [40–42]. However for quantum systems in higher dimensions, contracting the corresponding tensor networks is a $\#P$ -complete problem [43, 44]. This poses a significant challenge for the use of tensor network methods for quantum systems in two or more dimensions.

On the other hand, procedures making use of quantum devices to directly compute OTOCs have been proposed [45–49]. However many of these procedures require either specialised quantum systems to simulate specific Hamiltonians, or access to a universal fault-tolerant quantum computer (QC). In the latter case one would, in principle, be able to simulate arbitrary quantum many-body systems. However, the devices currently in operation are noisy intermediate-scale quantum (NISQ) devices [50], which cannot reliably operate at the large scales required in the aforementioned procedures. Accordingly, we need to explore new methods for accurately and efficiently determining OTOCs, and related quantities, in order to support continued research

in this direction.

In this work we investigate whether classical kernel methods (KMs) [51–53], powerful machine learning (ML) algorithms used for data analysis tasks, may help provide a solution to this problem. A previous work [54] applied restricted Boltzmann machines to learn early-time OTOCs, and gave one example of the procedure for the 2D transverse-field Ising model. Here we consider four parameterised sets of Hamiltonians, each containing a collection of 1D quantum systems which are studied in the condensed matter physics literature. For each set, we investigate whether classical KMs can be used to learn a specific OTOC, namely the XZ-OTOC, and a useful sum of OTOCs (defined in Section II C) as functions of the Hamiltonian parameters. We formulate the problem as a regression task, generating labelled data with an efficient numerical algorithm based on matrix product operators [41], for quantum many-body system sizes up to 40 qubits. The input data is given by uniform random samples of the Hamiltonian parameters drawn from a subset of the parameter space. The labels are given by either the value of the associated XZ-OTOC, or the sum of OTOCs. We split the generated data into training and testing sets and apply regularised empirical risk minimisation (RERM) [52, 53] with KMs. Using a variety of standard kernels, we perform a 10-fold cross-validation on the training data to find good hyperparameter values, and apply the best models to the testing data to assess their suitability for the problem.

The paper proceeds as follows. In Section II, we explain the necessary background material for discussing the ML tasks in detail, followed by a formal introduction to OTOCs and the associated sum of OTOCs on which we focus. In Section III, we describe the parameterised sets of Hamiltonians considered in this work and the associated ML tasks, together with the classical kernels which are applied to the ML problem. We then finish this section by discussing the methods used to generate the datasets. In Section IV, we report the numerical results, which include learning performance metrics for the best models making predictions on the training and testing sets for every problem instance. In Section V, we discuss the results and their significance. Finally, in Section VI, we conclude and provide suggestions for improving and extending our work in future research.

II. BACKGROUND

A. Regularised empirical risk minimisation

Supervised ML algorithms aim to find a function, called a *model*, that both accurately fits a training dataset of input-output pairs and makes accurate predictions for new data. However, if a model fits the training data too closely then it will often generalise poorly to unseen data, referred to as *overfitting*. This poses a challenge for supervised ML algorithms. The RERM method [52, 53] addresses this challenge by minimising a combination of the empirical risk, which measures performance on training data using a loss function, and a regularisation term. By including the regularisation term, RERM directly discourages overly intricate models, such as those that may arise from fitting noisy data exactly. This can help in finding a more robust model which is less prone to overfitting.

Let $\mathcal{D} = \{(\mathbf{x}_i, y_i)\}_{i=1}^M \subseteq \mathcal{X} \times \mathbb{R}$ be a *training dataset*, where $\mathcal{X} \equiv \mathbb{R}^d$ is the input data domain of dimension $d \in \mathbb{N}$, $\mathbf{x}_i \in \mathcal{X}$ is the i^{th} input training data sample, $y_i \in \mathbb{R}$ is the label for the i^{th} training data sample, and $M \in \mathbb{N}$ is the total number of training data samples. We denote the set of candidate models mapping $\mathcal{X} \rightarrow \mathbb{R}$, called the *hypothesis class*, by $\text{HYP}(\mathcal{X}, \mathbb{R})$. The *regularised empirical risk functional*, denoted $\mathcal{L}_{\mathcal{D}} : \text{HYP}(\mathcal{X}, \mathbb{R}) \rightarrow \mathbb{R}$, for \mathcal{D} is then defined by

$$\mathcal{L}_{\mathcal{D}}(f) = L_{\mathcal{D}}(f) + \lambda \Omega(f), \quad (1)$$

where $L_{\mathcal{D}} : \text{HYP}(\mathcal{X}, \mathbb{R}) \rightarrow \mathbb{R}$ is a *loss function* for \mathcal{D} , $\Omega : \text{HYP}(\mathcal{X}, \mathbb{R}) \rightarrow \mathbb{R}$ is the *regularisation term*, and $\lambda > 0$ is the *regularisation strength*. A common choice of the loss function for regression is given by the *mean squared error* (MSE), $L_{\mathcal{D}}(f) = \frac{1}{M} \sum_{i=1}^M (f(\mathbf{x}_i) - y_i)^2$. Similarly, common choices of the regularisation term include the l_1 -norm and the squared l_2 -norm of the model parameters, called Lasso and Tikhonov regularisation, respectively.

RERM for \mathcal{D} over $\text{HYP}(\mathcal{X}, \mathbb{R})$ is then the procedure of finding a model $f_{\text{opt}} \in \text{HYP}(\mathcal{X}, \mathbb{R})$ which minimises the regularised empirical risk functional for \mathcal{D} ,

$$f_{\text{opt}} = \arg \min_{f \in \text{HYP}(\mathcal{X}, \mathbb{R})} \mathcal{L}_{\mathcal{D}}(f). \quad (2)$$

By choosing λ in (1) to be strictly positive, called *regularisation*, we can sometimes help to bound the difference between the loss function for f_{opt} evaluated on the

training dataset, and the loss function for f_{opt} evaluated on unseen data [55]. This means that if RERM returns a model which accurately fits the training dataset, then the model will likely also perform well on unseen data, hence improving generalisation.

B. Kernel methods

When selecting an algorithm for a supervised ML task, several factors need to be considered. These include the dataset size and complexity, the type of problem (i.e., regression, classification, etc.), the efficiency of the training algorithm, and the availability of tools for implementation. KMs [51–53] are a collection of widely used ML algorithms aimed at capturing complex patterns in moderately sized datasets. The success of KMs stems largely from the use of kernel functions, which implicitly compute inner products between embeddings of input data in high-dimensional feature spaces. By utilising kernel functions, intricate non-linear structures in the original data can sometimes translate into standard linear functions in the feature space (see Figure 1). This simplification facilitates the learning process, making it considerably easier to identify the structures in the data, even with a small number of data points. Moreover, in many cases the training landscape for KMs is convex which enables the discovery of optimal model parameters via a deterministic procedure. This makes kernels a desirable candidate for a variety of supervised ML tasks.

Formally, a *kernel* is a symmetric function $\mathcal{K} : \mathcal{X} \times \mathcal{X} \rightarrow \mathbb{R}$ such that the *Gram matrix* $K_{ij} \equiv \mathcal{K}(x_i, x_j)$ of \mathcal{K} is positive semi-definite for all choices of the set $\{x_1, \dots, x_m\} \subseteq \mathcal{X}$ and all $m \in \mathbb{N}$. It can be shown (see Chapter 2.2 of [52]) that any kernel \mathcal{K} can be expressed in the form

$$\mathcal{K}(x, x') = \langle \phi(x), \phi(x') \rangle_{\mathcal{F}}, \quad (3)$$

for some function $\phi : \mathcal{X} \rightarrow \mathcal{F}$ and for all $x, x' \in \mathcal{X}$ (see Figure 1). The function $\phi : \mathcal{X} \rightarrow \mathcal{F}$ is called a *feature map* and its codomain \mathcal{F} is a Hilbert space over \mathbb{R} called a *feature space*. The kernel \mathcal{K} is then a measure of how similar two inputs are after being mapped into the feature space by ϕ .

Associated with each kernel \mathcal{K} is a Hilbert space over \mathbb{R} called the *reproducing kernel Hilbert space* (RKHS) of \mathcal{K} (Definition 2.9 in [52]), which we denote by $\mathcal{R}_{\mathcal{K}}$.

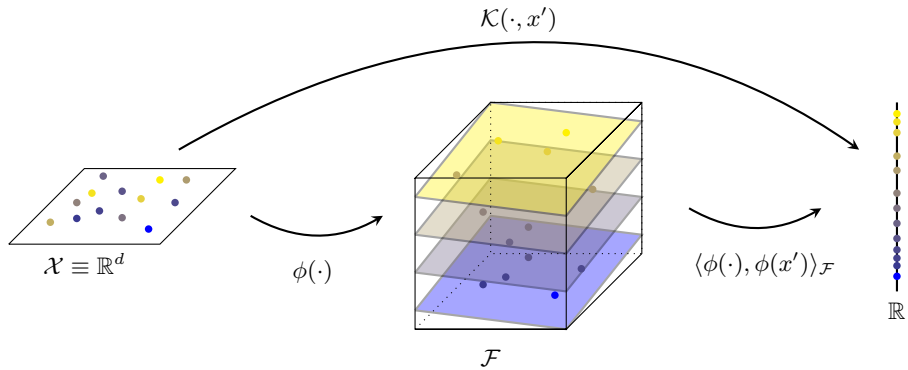


FIG. 1: A kernel function \mathcal{K} , which implicitly computes an inner-product in a high-dimensional feature space \mathcal{F} , can be used to simplify a regression problem if the associated feature map ϕ arranges the inputs in \mathcal{F} in a desirable way. For example, above we see points associated with different continuous labels (indicated by the varying colours) being arranged into different parallel hyperplanes.

This allows the continuous value associated with the points to be extracted via a simple projection along some axis in \mathcal{F} .

The RKHS $\mathcal{R}_{\mathcal{K}}$ is a space of functions mapping $\mathcal{X} \rightarrow \mathbb{R}$ defined such that

$$\mathcal{R}_{\mathcal{K}} \equiv \overline{\text{span}}_{\mathbb{R}} \{ \mathcal{K}(\cdot, x) | x \in \mathcal{X} \}. \quad (4)$$

That is, each $x \in \mathcal{X}$ is an index for a function $\mathcal{K}(\cdot, x)$ mapping $\mathcal{X} \rightarrow \mathbb{R}$, defined such that $x' \mapsto \mathcal{K}(x', x)$ for all $x' \in \mathcal{X}$. The span over \mathbb{R} of this collection of functions is itself a function space containing all real linear combinations of finitely many functions $\{ \mathcal{K}(\cdot, x_i) \}_{i=1}^m$ indexed by some subset $\{ x_i \}_{i=1}^m \subset \mathcal{X}$, where $m \in \mathbb{N}$. One can define an inner product for such linear combinations $f = \sum_{i=1}^m \alpha_i \mathcal{K}(\cdot, x_i)$ and $g = \sum_{j=1}^{m'} \beta_j \mathcal{K}(\cdot, x'_j)$ by

$$\langle f, g \rangle_{\mathcal{R}_{\mathcal{K}}} \equiv \sum_{i=1}^m \sum_{j=1}^{m'} \alpha_i \beta_j \mathcal{K}(x_i, x'_j). \quad (5)$$

The RKHS $\mathcal{R}_{\mathcal{K}}$ is then the completion of this function space with respect to the inner product in (5). Generally, an arbitrary element of the completed space $\mathcal{R}_{\mathcal{K}}$ cannot be written as a finite linear combination of kernel functions. However, under some weak conditions on \mathcal{X} and \mathcal{K} (see Lemma 4.33 in [51]), we can write an arbitrary model $f \in \mathcal{R}_{\mathcal{K}}$ as a countable sum,

$$f(\cdot) = \sum_{i \in \mathbb{N}} \alpha_i \mathcal{K}(\cdot, x_i), \quad (6)$$

for some $\alpha_i \in \mathbb{R}$ and $x_i \in \mathcal{X}$.

Performing RERM with KMs amounts to choosing an appropriate kernel \mathcal{K} and using the corresponding RKHS $\mathcal{R}_{\mathcal{K}}$ as the hypothesis class, whose elements can be written as in (6). Optimisation over this space would appear to require searching for the best choice of infinitely many real coefficients $\{\alpha_i\}_{i \in \mathbb{N}}$. However, the *representer theorem* (Theorem 4.2 in [52] and Theorem 6.11 in [53]) reduces the problem to a finite-dimensional one. Suppose that we have a finite training dataset $\mathcal{D} = \{(\mathbf{x}_i, y_i)\}_{i=1}^M \subseteq \mathcal{X} \times \mathbb{R}$ and a regularisation term $\Omega(f) = g(\|f\|_{\mathcal{R}_{\mathcal{K}}})$, where $g : [0, \infty) \rightarrow \mathbb{R}$ is some strictly increasing function, and $\|\cdot\|_{\mathcal{R}_{\mathcal{K}}}$ is the norm induced by the inner product on $\mathcal{R}_{\mathcal{K}}$. Under these conditions, the representer theorem states that the functions in $\mathcal{R}_{\mathcal{K}}$ which minimise the regularised empirical risk functional can be expressed in the form

$$f(\cdot) = \sum_{i=1}^M \alpha_i \mathcal{K}(\cdot, \mathbf{x}_i). \quad (7)$$

Notice that (7) involves only finitely many real coefficients $\{\alpha_i\}_{i=1}^M$ which define a linear combination of finitely many functions $\{\mathcal{K}(\cdot, \mathbf{x}_i)\}_{i=1}^M$ associated with the input training data $\{\mathbf{x}_i\}_{i=1}^M$.

Therefore, we can find the minimisers of the regularised empirical risk functional by searching over the finite-dimensional space of coefficients $\vec{\alpha} = (\alpha_i)_{i=1}^M \in \mathbb{R}^M$. Further, if the regularised empirical risk functional is convex, then the optimal $\vec{\alpha}$ is unique and we can compute it deterministically. In this work, we use the

MSE loss function and the regularisation term defined by $\Omega(f) = \frac{1}{M} \|f\|_{\mathcal{R}_K}^2$ for all $f \in \mathcal{R}_K$. In this case the regularised empirical risk functional is convex (see Appendix A.1). From this, it can be shown (see Appendix A.2) that the optimal $\vec{\alpha} \in \mathbb{R}^M$ is given by

$$\vec{\alpha} = (K^2 + \lambda K)^+ K \vec{y}, \quad (8)$$

where $\vec{y} = (y_i)_{i=1}^M \in \mathbb{R}^M$ is the vector of training data labels, $K_{ij} = \mathcal{K}(\mathbf{x}_i, \mathbf{x}_j)$ is the *kernel matrix* for the input training data $\{\mathbf{x}_i\}_{i=1}^M$, and $(\cdot)^+$ is the Moore-Penrose pseudoinverse [56].

From (8), we see that determining the optimal $\vec{\alpha} \in \mathbb{R}^M$ requires the Moore-Penrose pseudoinverse of the $M \times M$ matrix $K^2 + \lambda K$ to be known. The time complexity of calculating the pseudoinverse of a square matrix, which is the most computationally expensive part of this algorithm, is cubic in the number of rows or columns. This implies that the time complexity of training a model with this algorithm scales as $\mathcal{O}(M^3)$ with the size of the training data set $M \in \mathbb{N}$. Once the optimal $\vec{\alpha}$ has been determined, (7) shows that the time-complexity of predicting the label for a new input scales as $\mathcal{O}(M)$. Accordingly, it is important for the size of the training dataset to be reasonably small, otherwise the time required for training (and making predictions) can become prohibitively large. Similarly, we need to be able to compute the kernel \mathcal{K} efficiently, otherwise both calculating the kernel matrix entries and making predictions could be computationally expensive. The procedures for determining the optimal model (i.e. training) and making predictions for new input data are summarised in Algorithm 1 and Algorithm 2, respectively. These are the algorithms which we apply to the learning problems considered in this work.

Algorithm 1 Training a regression model with kernel methods

Inputs: Training dataset $\mathcal{D} = \{(\mathbf{x}_i, y_i)\}_{i=1}^M$, kernel \mathcal{K} , regularisation strength λ

Output: Coefficients $\vec{\alpha} \in \mathbb{R}^M$ of the model in (7) that solves RERM for \mathcal{D} over \mathcal{R}_K

```

1: for  $i = 1, \dots, M$  do
2:   for  $j = 1, \dots, M$  do
3:     Set  $K_{ij} := \mathcal{K}(\mathbf{x}_i, \mathbf{x}_j)$ 
4:   end for
5: end for
6: Calculate  $\vec{\alpha}$  according to (8)
7: return  $\vec{\alpha}$ 
```

Algorithm 2 Making a prediction using a trained regression model with kernel methods

Inputs: Input data sample $x \in \mathcal{X}$, input training data $\{\mathbf{x}_i\}_{i=1}^M$, kernel \mathcal{K} , coefficients $\vec{\alpha} \in \mathbb{R}^M$ output by Algorithm 1

Output: Predicted label $y \in \mathbb{R}$ associated with the input data sample $x \in \mathcal{X}$

```

1: Set  $y := 0$ 
2: for  $i = 1, \dots, M$  do
3:   Set  $y := y + \alpha_i \mathcal{K}(x, \mathbf{x}_i)$ 
4: end for
5: return  $y$ 
```

C. Information Spreading and Out-of-Time-Ordered Correlators

We now consider the question of how one may quantify the spread of information in quantum many-body systems. One way to make this concrete is to consider how one could use the natural dynamics of a quantum system to transmit information [15]. Consider an n -qubit quantum system evolving under a time-independent local Hamiltonian H . Let V_j, W_k denote 1-qubit Pauli operators $V, W \in \{X, Y, Z\}$ which act only on qubits $j, k \in \{1, \dots, n\}$, respectively. Suppose Alice has access to qubit j and Bob has access to qubit k . Alice wants to send a classical bit $a \in \{0, 1\}$ to Bob, and does so by either applying V_j at $t = 0$ if $a = 1$, or does nothing if $a = 0$. The system then evolves for some time t , after which Bob measures W_k and attempts to determine whether V_j was applied (see Figure 2).

If the system begins in the state described by the density operator ρ , then we can use the Cauchy-Schwarz inequality to bound the difference between the expectation values that Bob measures in each case [15]. In particular,

$$\begin{aligned} & |\langle V_j W_k(t) V_j \rangle_\rho - \langle W_k(t) \rangle_\rho|^2 \\ & \leq \langle [V_j, W_k(t)]^\dagger [V_j, W_k(t)] \rangle_\rho, \end{aligned} \quad (9)$$

where $W_k(t) \equiv e^{iHt} W_k e^{-iHt}$ is the operator W_k evolved in the Heisenberg picture, and $\langle \cdot \rangle_\rho$ denotes the expectation value measured from the state ρ . The right-hand side of (9) is a measure of the size of the commutator $[V_j, W_k(t)]$ in the state ρ . If ρ is the maximally mixed state $\mathbb{I}^{\otimes n}/2^n$, where \mathbb{I} is the 2×2 identity matrix, then the right-hand side is proportional to the square of the

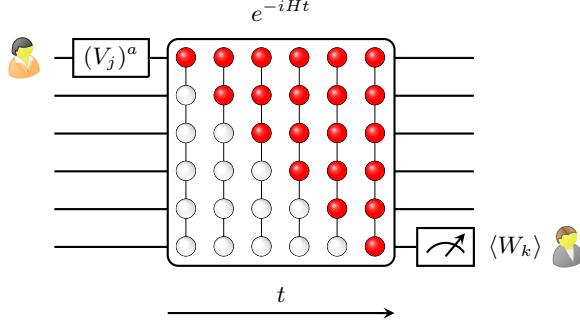


FIG. 2: The Alice-Bob classical communication protocol in the case where the system is a 1D spin chain with open boundary conditions, evolving under a time-independent local Hamiltonian H . Alice and Bob have access to the individual qubits at opposite ends of the chain. Alice wants to send a bit $a \in \{0, 1\}$ to Bob by applying V_j if $a = 1$, or doing nothing if $a = 0$. The system then evolves for a time t , during which the influence of

Alice's operation propagates through the system. Bob then performs a measurement of W_k to try and determine the value of the bit a .

Frobenius norm of the operator $[V_j, W_k(t)]$. Thus, we see that the size of this commutator bounds the sensitivity of the expectation value of $W_k(t)$ to the initial perturbation V_j . If the commutator is small, then Alice and Bob would need to repeat the procedure many times in order for Bob to reliably distinguish between the two cases, and hence determine which bit was sent.

One can gain further insight into how information spreads in the system by examining the Heisenberg evolution of local observables. Specifically, the Heisenberg time evolution of W_k can be expanded as

$$W_k(t) = W_k + \sum_{l=1}^{\infty} \frac{(it)^l}{l!} \underbrace{[H, \dots, [H, [H, W_k]] \dots]}_{l \text{ times}}. \quad (10)$$

If the Hamiltonian H only contains local (e.g. nearest-neighbour) interactions, then the number of sites upon which the nested commutators act non-trivially generally increases with the sum index l in (10). The operator $W_k(t)$ is thus highly non-local in general. However, for small $|t|$, the terms in the sum with large support (i.e. large l) are insignificant and only become significant as $|t|$ increases. This gradual increase in the magnitude of the non-local terms describes how $W_k(t)$ spreads to become increasingly non-local over time. The extent to which $W_k(t)$ fails to commute with an operator V_j then depends on the magnitude of the terms in (10) which

do not simply contain the identity operator on qubit j (i.e. those with support on qubit j).

These considerations suggest quantifying the spread of information in terms of the size of commutators between local operators in the Heisenberg picture. To this end, we define the *OTOC* as follows. Firstly, the *squared-commutator OTOC* [28, 57], denoted $C_{jk}(t)$, is the non-negative real number defined such that

$$C_{jk}(t) \equiv \frac{1}{2} \langle [V_j, W_k(t)]^\dagger [V_j, W_k(t)] \rangle_{\mathbb{I}^{\otimes n}/2^n}. \quad (11)$$

As mentioned above, the expression in (11) is proportional to the square of the Frobenius norm of the operator $[V_j, W_k(t)]$, and thus captures the size of this commutator. Since V_j and W_k are both Hermitian and unitary, one can expand the commutators in (11) to write $C_{jk}(t) = 1 - F_{jk}(t)$, where $F_{jk}(t)$ is the real number given by

$$F_{jk}(t) \equiv \langle V_j W_k(t) V_j W_k(t) \rangle_{\mathbb{I}^{\otimes n}/2^n}. \quad (12)$$

The latter quantity, $F_{jk}(t)$, will be referred to as simply the *OTOC* [14, 15, 31]. Note that the OTOC and squared-commutator OTOC are sometimes defined via an expectation value measured from an arbitrary state. However, for the purposes of this paper we will take them to be defined by an expectation value measured from the maximally mixed state $\mathbb{I}^{\otimes n}/2^n$, which ensures that $F_{jk}(t)$ is real.

Equation (9) illustrates how the OTOC bounds the transmission of classical information in a quantum system, but the OTOC can also be used to study the transmission of quantum information. This is often investigated in the setup of the Hayden-Preskill protocol, which is a toy model for studying the recovery of information from black holes [7]. Similar to above, we consider an isolated n -qubit system, which we denote by \mathcal{S} . Alice has access to a qubit q_A in \mathcal{S} , and Bob has access to a qubit q_B , also in \mathcal{S} . Instead of applying an operation to q_A as before, Alice will prepare q_A in a state which is maximally entangled with another reference system R_1 ,

$$|\psi\rangle_{q_A \cup R_1} = \frac{1}{\sqrt{2}}(|00\rangle + |11\rangle). \quad (13)$$

The remainder of the system, $\mathcal{S} - q_A$, is prepared in the maximally mixed state, $\rho_{\mathcal{S} - q_A} = \mathbb{I}^{\otimes n-1}/2^{n-1}$. Since \mathcal{S} is a closed system, the reference system R_1 remains

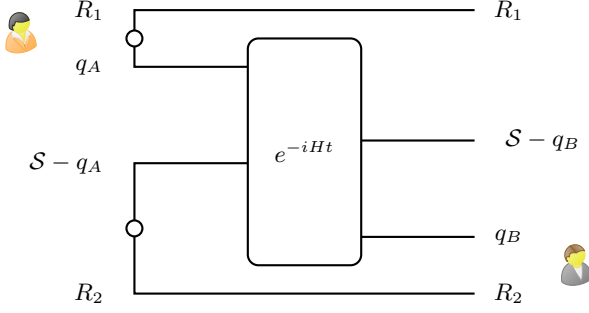


FIG. 3: Tensor network representation of the systems involved in the Alice-Bob quantum communication protocol. Initially, subsystems R_1 and q_A form a Bell state, while subsystems $\mathcal{S} - q_A$ and R_2 form $n - 1$ Bell states. The unitary operator e^{-iHt} is then applied to the system \mathcal{S} . Bob's aim is to detect and quantify the entanglement with R_1 that has spread from q_A to q_B .

maximally entangled with \mathcal{S} as the system evolves in time. Initially, R_1 is only entangled with the subsystem q_A , but as q_A interacts with the rest of the system, the entanglement with R_1 generally spreads into the non-local degrees of freedom of \mathcal{S} . One can track the spreading of entanglement by examining to what extent Bob is able to recover the entanglement with R_1 from another qubit, such as q_B , in \mathcal{S} .

In the Hayden-Preskill protocol, Bob is also given access to a reference system introduced to purify the subsystem $\mathcal{S} - q_A$ [7]. Since $\mathcal{S} - q_A$ begins in a maximally mixed state, it can be purified with another $(n - 1)$ -qubit reference system R_2 , with which $\mathcal{S} - q_A$ forms $n - 1$ Bell pairs,

$$|\psi\rangle_{(\mathcal{S} - q_A) \cup R_2} = \frac{1}{2^{(n-1)/2}} (|00\rangle + |11\rangle)^{\otimes(n-1)}. \quad (14)$$

Figure 3 shows a tensor network representation of the various systems involved, where \circ indicates that the subsystems form a collection of Bell pairs. The amount of information that Bob has about R_1 can then be quantified by the mutual information,

$$I(R_1 : q_B \cup R_2) \equiv S(R_1) + S(q_B \cup R_2) - S(R_1 \cup q_B \cup R_2), \quad (15)$$

where $S(A) \equiv -\text{Tr}(\rho_A \log_2 \rho_A)$ is the von Neumann entropy of the reduced state ρ_A of a general subsystem A . The mutual information $I(R_1 : q_B \cup R_2)$ is importantly also related to the coherent information $I(R_1 \rangle q_B \cup R_2)$ of the induced channel from q_A to $q_B \cup R_2$, which in

turn is related to the quantum capacity of the channel [58, 59]. Indeed, from a simple application of the definition of $I(R_1 \rangle q_B \cup R_2)$ it is easy to verify that

$$I(R_1 \rangle q_B \cup R_2) = I(R_1 : q_B \cup R_2) - 1, \quad (16)$$

where we have used $S(R_1) = 1$.

How can the OTOC be used to understand the spreading of entanglement? To this end, it can be shown (see Section IV.A in [15]) that the OTOC provides a lower bound on the mutual information,

$$I(R_1 : q_B \cup R_2) \geq 4 - \log_2 \left(7 + \sum_{\substack{V, W \\ \in \{X, Y, Z\}}} \frac{1}{2^n} \text{Tr} \left((V_{q_B} W_{q_A}(-t))^2 \right) \right). \quad (17)$$

The sum appearing in the right-hand side of (17) is a sum of OTOCs for different choices of $V, W \in \{X, Y, Z\}$ acting on qubits q_B and q_A , respectively. From this inequality, we can clearly see the role that the OTOC plays in detecting how much information about R_1 has propagated from q_A to q_B . For instance, at $t = 0$ the operators $W_{q_A}(0)$ and V_{q_B} commute, so each term in the sum above is equal to 1, yielding a trivial lower bound of $I(R_1 : q_B \cup R_2) \geq 0$. However, as time progresses, the support of $W_{q_A}(-t)$ will generally grow to include qubit q_B so that $W_{q_A}(-t)$ and V_{q_B} no longer commute. When this happens, the OTOC values begin to decay from 1, causing the right-hand side of (17) to be strictly greater than 0. This allows Bob to infer that at least some information about R_1 has reached q_B , and gives him a lower bound on how much information he possesses.

Beyond simply determining how much information has reached q_B , in [60] an efficient decoding procedure was proposed for recovering the entanglement with R_1 , by applying a unitary operation on $q_B \cup R_2$ to reconstruct a Bell state on $R_1 \cup q_B$. The fidelity of the decoding protocol is closely related to the sum of OTOCs appearing in (17). Because of the importance of this sum in determining the spreading of quantum information through a quantum many-body system, in the following sections we will investigate how to compute its value in different systems using kernel machines.

III. METHODS

The manner in which information propagates through the system \mathcal{S} depends on the details of its dynamics, which is specified by the time-independent Hamiltonian H . This means that in order to compute OTOCs and related quantities, such as the sum of OTOCs in (17), generally we need to simulate the evolution of the system \mathcal{S} . This amounts to calculating e^{-iHt} . Such a calculation becomes computationally intensive for a generic H as the size of the system increases, and needs to be performed for every H and value of time t that one wishes to investigate. In spite of this, is there some property of many-body Hamiltonians that can be used to determine OTOCs without the need to simulate the full dynamics? Here we investigate whether such properties may be captured by a ML model which makes use of KMs as described in Algorithms 1 and 2. In this section we describe the methods used to conduct the investigation. This includes a description of the parameterised sets of Hamiltonians we consider, how the task is framed as a learning problem, the specific kernels which are trained and applied to the data, and the techniques used to generate the data.

A. The parameterised sets of Hamiltonians

The learning problem addressed in this work requires us to choose a parameterised set of Hamiltonians $\{H(x) : x \in \mathbb{R}^d\}$ to investigate. This determines both the set of possible dynamics for \mathcal{S} , and the explicit form of the OTOCs considered in the learning problem. With this in mind, we consider 4 distinct choices of the parameterised set of n -qubit Hamiltonians. Each of the sets forms a 3-dimensional (i.e., $d = 3$) subspace of Hermitian operators describing a collection of 1D quantum systems. The parameterised sets are chosen to contain systems which are widely considered in condensed matter physics.

The first set of Hamiltonians, denoted $\mathcal{H}_1 = \{H_1(x) :$

$x \in \mathbb{R}^3\}$, has elements $H_1(x)$ defined by

$$H_1(x) = x_1 \left(\sum_{i=1}^n X_i \right) + x_2 \left(\sum_{j=1}^{n-1} X_j X_{j+1} \right) + x_3 \left(\sum_{k=1}^{n-2} Z_k X_{k+1} Z_{k+2} \right) \quad (18)$$

for all $x = (x_1, x_2, x_3) \in \mathbb{R}^3$. The ground states of the Hamiltonians in \mathcal{H}_1 exhibit a $\mathbb{Z}_2 \times \mathbb{Z}_2$ symmetry-protected topological phase that is considered in the machine learning articles [61, 62], and motivates our consideration of the set here.

The second set, denoted $\mathcal{H}_2 = \{H_2(x) : x \in \mathbb{R}^3\}$, is often called the XYZ Heisenberg model [63–66] and has elements $H_2(x)$ defined by

$$H_2(x) = x_1 \left(\sum_{i=1}^{n-1} X_i X_{i+1} \right) + x_2 \left(\sum_{j=1}^{n-1} Y_j Y_{j+1} \right) + x_3 \left(\sum_{k=1}^{n-1} Z_k Z_{k+1} \right) \quad (19)$$

for all $x = (x_1, x_2, x_3) \in \mathbb{R}^3$. The Hamiltonians in \mathcal{H}_2 serve as quantum models of ferromagnetic and anti-ferromagnetic materials. Specifically, they describe 1D spin-chains with nearest-neighbour spin couplings. In the case $x_1, x_2, x_3 > 0$, this model captures the tendency of neighbouring atoms in anti-ferromagnetic materials to align their atomic magnetic moments in an anti-parallel fashion when occupying low-energy states. For $x_1, x_2, x_3 < 0$, the spins tend to align, which models ferromagnetic materials.

The third set, denoted $\mathcal{H}_3 = \{H_3(x) : x \in \mathbb{R}^3\}$, is a generalised version of the Majumdar-Ghosh model [67–70] and has elements $H_3(x)$ defined by

$$H_3(x) = x_1 \left(\sum_{i=1}^{n-1} X_i X_{i+1} + 0.5 \sum_{j=1}^{n-1} X_j X_{j+2} \right) + x_2 \left(\sum_{i=1}^{n-1} Y_i Y_{i+1} + 0.5 \sum_{j=1}^{n-1} Y_j Y_{j+2} \right) + x_3 \left(\sum_{i=1}^{n-1} Z_i Z_{i+1} + 0.5 \sum_{j=1}^{n-1} Z_j Z_{j+2} \right) \quad (20)$$

for all $x = (x_1, x_2, x_3) \in \mathbb{R}^3$. Similar to \mathcal{H}_2 , the Hamiltonians in \mathcal{H}_3 provide quantum models of ferromagnetic and anti-ferromagnetic materials. They also describe 1D spin-chains with nearest-neighbour spin couplings, in addition to next-nearest neighbour spin-couplings, where the relative magnitude of the next-nearest-neighbour couplings are half as great as the nearest-neighbour couplings. This is a slightly more realistic model of anti-ferromagnetic and ferromagnetic materials which does not assume that atoms only interact with their nearest-neighbours.

The fourth and final set, denoted $\mathcal{H}_4 = \{H_4(x) : x \in \mathbb{R}^3\}$, is often called the mixed-field Ising chain [71–73] and has elements defined by

$$H_4(x) = x_1 \left(\sum_{i=1}^n X_i \right) + x_2 \left(\sum_{i=1}^n Z_i \right) + x_3 \left(\sum_{k=1}^{n-1} Z_k Z_{k+1} \right) \quad (21)$$

for all $x = (x_1, x_2, x_3) \in \mathbb{R}^3$. The Hamiltonians in this set describe a semi-classical version of the 1D Ising chain under the influence of an external homogenous magnetic field with non-zero components in the physical x and z directions.

With reference to equations (18), (19), (20) and (21), when we evolve a quantum system according to the unitary operator $e^{-iH_j(x)}$ (where $j \in \{1, 2, 3, 4\}$), the evolution time t is effectively quantified by the Euclidean norm $\|x\|$ of the parameter vector $x \in \mathbb{R}^3$. This means that limiting the evolution time of the associated quantum systems corresponds to restricting the norm of the parameter vector $x \in \mathbb{R}^3$. Accordingly, it is most natural to sample the input data (i.e., the parameter vectors) from a ball in \mathbb{R}^3 centered at the origin, whose radius determines the maximum evolution time.

For \mathcal{H}_1 , \mathcal{H}_2 and \mathcal{H}_3 , we chose to uniformly sample input data from the ball of radius n centered at the origin. This means that the effective evolution time t of the corresponding n -qubit quantum systems is bounded above by $t \leq n$. This is motivated by both computational budgets and empirical observations from initial simulations, which showed that linear time in the system size is sufficient to exhibit interesting behaviours or dynamics in the system (see Figures 4(a)–(c)). For \mathcal{H}_4 , we chose to uniformly sample input data from the ball of radius $2n$ centered at the origin. Increasing the radius of the ball for \mathcal{H}_4 was motivated by the observation that sampling from the ball of radius n did not produce much variation in the value of the OTOCs we consider (see Figure 4(d)). Informally, one possible explanation for this is that the only term in (21) which contributes to the spread of information is the term multiplied by x_3 , and this term only transfers information about Z to neighbouring qubits. In contrast, the terms in the Hamiltonians in \mathcal{H}_1 , \mathcal{H}_2 and \mathcal{H}_3 that contribute to the spread of information collectively transfer at least Z and X information. Accordingly, it seems reasonable that the systems in \mathcal{H}_4 require a greater maximum evolution time to observe changes in the correlations captured by the OTOC.

B. The learning problem

In order to formulate the problem as a learning task, we consider one of the parameterised sets of Hamiltonians $\mathcal{H} = \{H(x) : x \in \mathbb{R}^d\}$, and set up ML models to learn two distinct functions of the Hamiltonian parameters $x \in \mathbb{R}^d$. The first function, denoted $\mathcal{O}_{XZ} : \mathbb{R}^d \rightarrow \mathbb{R}$, captures the XZ-OTOC when $j = n$ and $k = 1$ (i.e., $W = Z$ on the first qubit and $V = X$ on the last qubit in the 1D spin-chain). Specifically, \mathcal{O}_{XZ} is defined such that

$$\mathcal{O}_{XZ}(x) = \frac{1}{2^n} \text{Tr} (X_n \mathcal{Z}_1(x) X_n \mathcal{Z}_1(x)) \quad (22)$$

for all $x \in \mathbb{R}^d$, where we denote by $\mathcal{Z}_1(x) \equiv e^{iH(x)} Z_1 e^{-iH(x)}$ the operator Z_1 evolved in the Heisenberg picture under $H(x)$ for one unit of time. The Hamiltonian parametrisations that we consider have the property $H(tx) = tH(x)$ for any $t \in \mathbb{R}$, hence we simply absorb the evolution time t into the Euclidean norm of $x \in \mathbb{R}^d$.

The second function, denoted $\mathcal{O}_{Sum} : \mathbb{R}^d \rightarrow \mathbb{R}$, captures the sum of OTOCs in (17) when q_A and q_B lie at opposite ends of the 1D spin chain, and is given by

$$\mathcal{O}_{Sum}(x) = \sum_{V,W \in \{X,Y,Z\}} \frac{1}{2^n} \text{Tr} (V_n \mathcal{W}_1(x) V_n \mathcal{W}_1(x)), \quad (23)$$

where we denote $\mathcal{W}_1(x) \equiv e^{-iH(x)} W_1 e^{iH(x)}$. Note that the signs of the exponents in the definition of $\mathcal{W}_1(x)$ have been reversed to account for the minus sign in the arguments of the Heisenberg operators in (17).

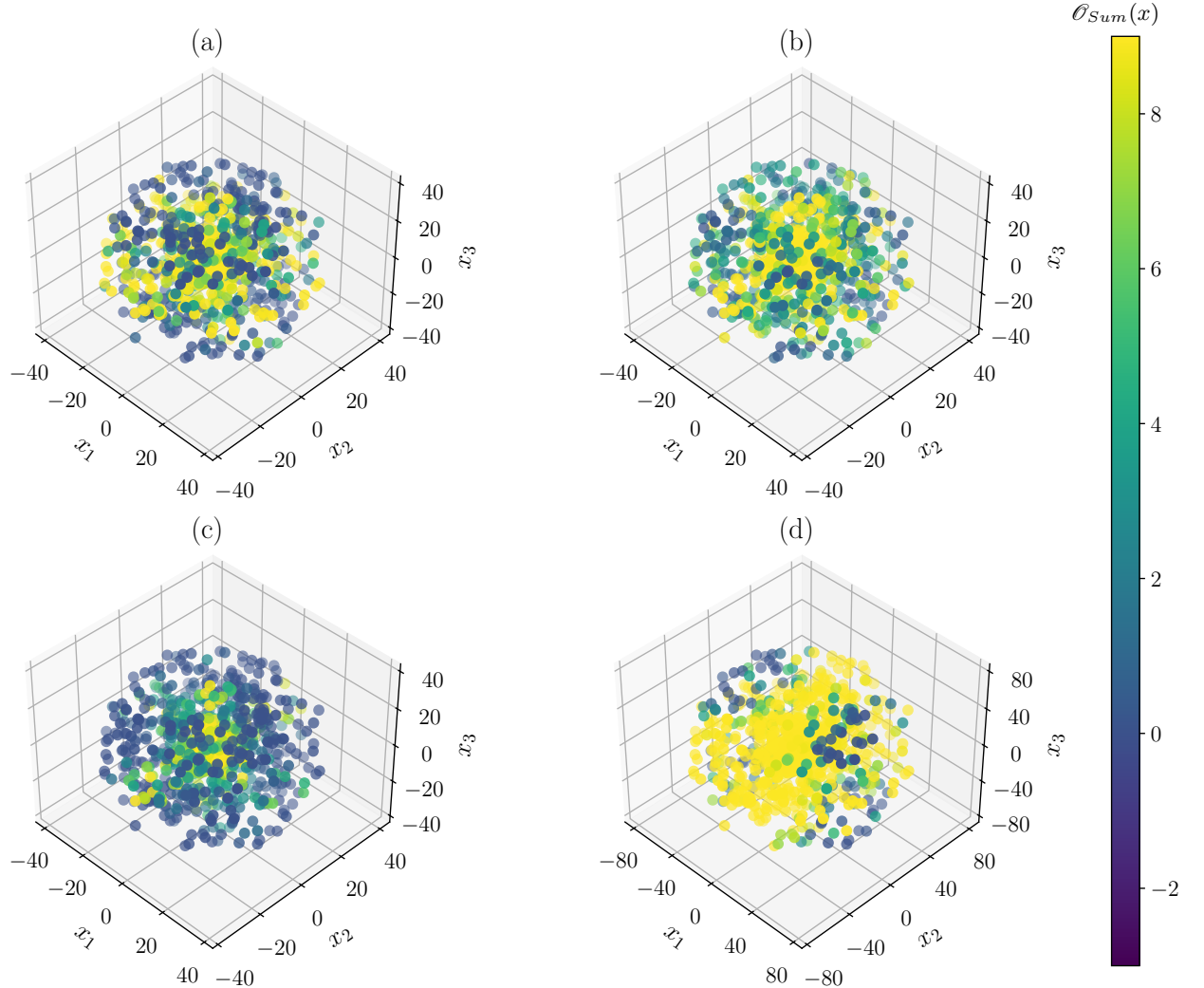


FIG. 4: Scatter plot of the 40-qubit training data for \mathcal{O}_{Sum} . The colour of a point at (x_1, x_2, x_3) specifies the value of $\mathcal{O}_{Sum}(x_1, x_2, x_3)$ as calculated with the MPO-based algorithm. The plots display the \mathcal{O}_{Sum} training data for \mathcal{H}_1 in (a), \mathcal{H}_2 in (b), \mathcal{H}_3 in (c), and \mathcal{H}_4 in (d).

The learning task is then to find a model which accurately learns \mathcal{O}_{XZ} or \mathcal{O}_{Sum} from sampled data (we describe our procedure for generating data in Section III D). In total, we consider 64 instances of the learning task: one for each choice of \mathcal{O}_{XZ} or \mathcal{O}_{Sum} , with one of the four parameterised sets of Hamiltonians \mathcal{H} from Section III A, and a system size of 5, 10, 15, 20, 25, 30, 35 or 40 qubits. For each of the tasks, we

examine 6 different choices of kernel functions (see Section III C) and compare their performance by determining how well the models perform on unseen test data. Thus, the generated data is split into training and testing data, 80% for training and 20% for testing. Next we perform a 10-fold cross validation on the training data to find suitable hyperparameter values for the various kernels using a grid-search. The hyperparameter values

which we trial are listed in Table I of Appendix B. The best hyperparameter values are then selected based on the average coefficient of determination (R^2) over all 10 folds of the training data, and are used to train and apply ML models to the testing data. The best hyperparameter values for every instance of the learning task can be found in Tables II–V of Appendix B.

C. The kernels

We now provide definitions of the 6 kernels which are used to train ML models and make predictions on the testing sets for each problem instance. Some of the kernels depend on hyperparameters $\gamma \in \mathbb{R}$, $c_0 \in \mathbb{R}$ and $d \in \mathbb{N}$ which, as discussed above, are tuned via a 10-fold cross-validation on the training data (see Section III B). The first kernel is the *linear kernel*, denoted $\mathcal{K}_{\text{lin}} : \mathcal{X} \times \mathcal{X} \rightarrow \mathbb{R}$, which is defined by the standard Euclidean inner product of its arguments,

$$\mathcal{K}_{\text{lin}}(x, x') = \langle x, x' \rangle. \quad (24)$$

The second is the *polynomial kernel*, denoted $\mathcal{K}_{\text{poly}} : \mathcal{X} \times \mathcal{X} \rightarrow \mathbb{R}$, defined such that

$$\mathcal{K}_{\text{poly}}(x, x') = (\gamma \langle x, x' \rangle + c_0)^d. \quad (25)$$

The third is the *radial basis function (RBF) kernel*, denoted $\mathcal{K}_{\text{RBF}} : \mathcal{X} \times \mathcal{X} \rightarrow \mathbb{R}$, defined such that

$$\mathcal{K}_{\text{RBF}}(x, x') = e^{-\gamma \|x - x'\|^2}, \quad (26)$$

where $\|\cdot\|$ is the standard Euclidean norm. The fourth is the *Laplacian kernel*, denoted $\mathcal{K}_{\text{Lap}} : \mathcal{X} \times \mathcal{X} \rightarrow \mathbb{R}$, defined such that

$$\mathcal{K}_{\text{Lap}}(x, x') = e^{-\gamma \|x - x'\|_1}, \quad (27)$$

where $\|\cdot\|_1$ is the l_1 norm. The fifth is the *sigmoid kernel*, denoted $\mathcal{K}_{\text{sig}} : \mathcal{X} \times \mathcal{X} \rightarrow \mathbb{R}$, defined such that

$$\mathcal{K}_{\text{sig}}(x, x') = \tanh(\gamma \langle x, x' \rangle + c_0). \quad (28)$$

And the sixth kernel is the *cosine kernel*, denoted $\mathcal{K}_{\text{cos}} : \mathcal{X} \times \mathcal{X} \rightarrow \mathbb{R}$, defined such that

$$\mathcal{K}_{\text{cos}}(x, x') = \frac{\langle x, x' \rangle}{\|x\| \|x'\|}. \quad (29)$$

Each of these kernels are commonly used in ML algorithms that apply KMs to regression problems, which lead to our use of them here. Additionally, the Scikit Learn Python package [74] has a function `pairwise_kernels` for conveniently calculating the associated kernel matrices. Using this function, the 10-fold cross-validation for the regularisation strength λ and the other hyperparameters $\gamma \in \mathbb{R}$, $c_0 \in \mathbb{R}$ and $d \in \mathbb{N}$ is performed.

D. Generating the data

To generate the data for this work, we use an efficient numerical algorithm based on matrix product operators (MPOs) [41]. Specifically, we sample inputs x from subsets of \mathbb{R}^3 (see Section III A), which effectively selects a Hamiltonian $H(x)$ from one of the sets \mathcal{H} . We then directly calculate the associated labels determined by \mathcal{O}_{XZ} and \mathcal{O}_{Sum} with the MPO-based algorithm. This involves representing each of the operators under the trace in (22) and (23) as an MPO, and evolving them in the Heisenberg picture using time-evolving block decimation (TEBD) [75, 76].

Applying the algorithm requires us to choose an appropriate maximum bond dimension χ for the MPOs. A larger χ makes the algorithm more computationally expensive to implement, but also means that the computed numerical values are generally more accurate. Accordingly, we need to pick a bond dimension that both fits within the computational budget, and leads to reasonably accurate labels for the data points. In Figure 5, we provide plots of some of the labels for the 40-qubit systems against the value of χ used to calculate them, which shows how well the labels have converged with respect to the bond dimensions selected for producing the datasets. In an attempt to balance the trade-off between compute costs and convergence, we chose to use a maximum bond dimension χ of 110, 140, 110 and 150 to calculate the values of the function \mathcal{O}_{XZ} with \mathcal{H}_1 , \mathcal{H}_2 , \mathcal{H}_3 and \mathcal{H}_4 , respectively. Similarly, we chose to use a maximum bond dimension χ of 70, 90, 70 and 100 to calculate the values of the function \mathcal{O}_{Sum} with \mathcal{H}_1 , \mathcal{H}_2 , \mathcal{H}_3 and \mathcal{H}_4 , respectively.

In addition to this selection of bond dimensions, we use a Trotter step size of $\Delta t = 0.05$ to perform the Heisenberg picture time evolution of the MPOs using TEBD. This seems reasonable when one considers that

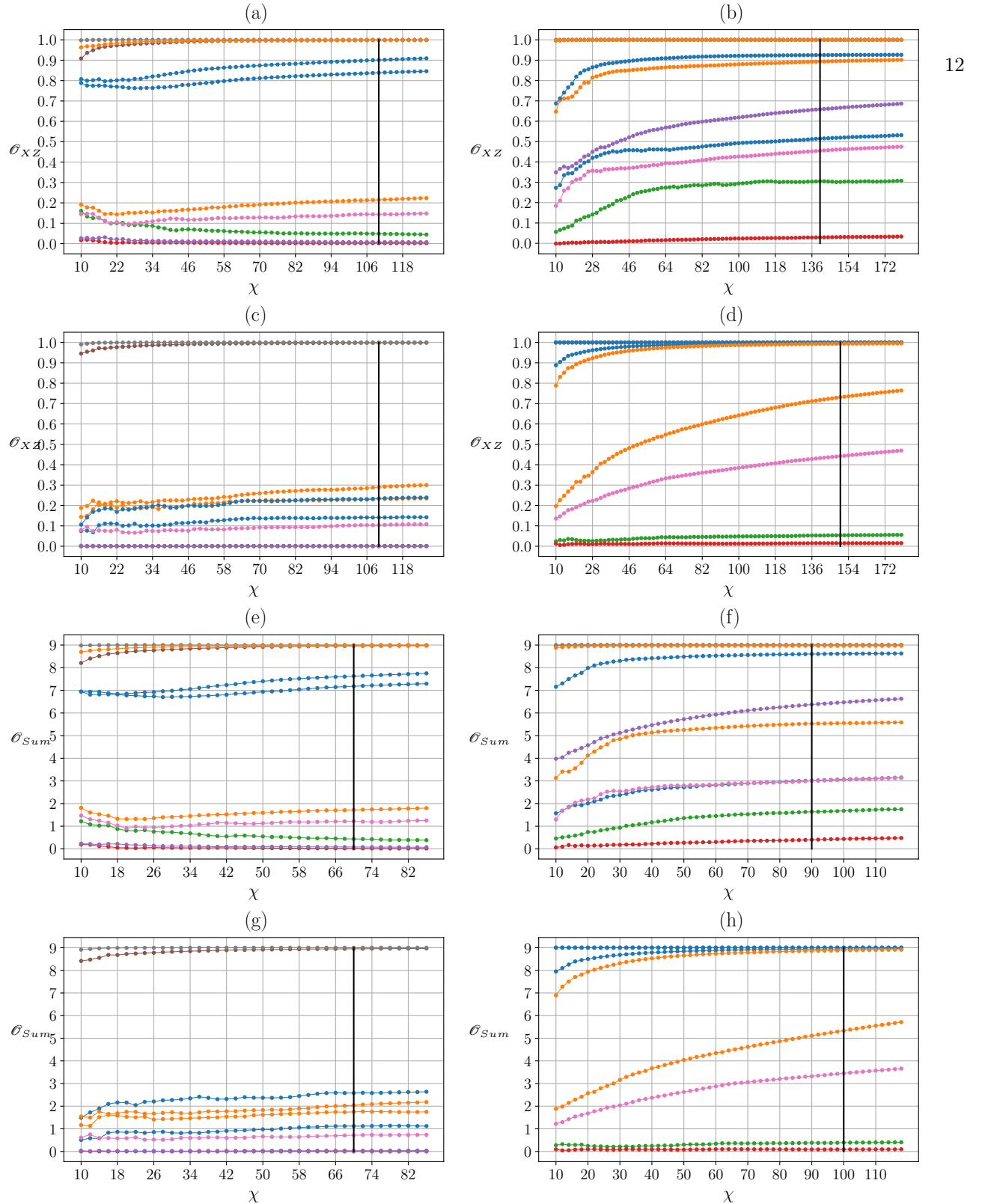


FIG. 5: The numerical values of \mathcal{O}_{XZ} and \mathcal{O}_{Sum} for 10 randomly sampled inputs plotted against the maximum bond dimension χ used to calculate them for 40-qubit quantum systems. Plots (a), (b), (c) and (d) show \mathcal{O}_{XZ} with $\mathcal{H}_1, \mathcal{H}_2, \mathcal{H}_3$ and \mathcal{H}_4 , respectively. Plots (e), (f), (g) and (h) show \mathcal{O}_{Sum} with $\mathcal{H}_1, \mathcal{H}_2, \mathcal{H}_3$ and \mathcal{H}_4 , respectively. The vertical black lines indicate the value of χ used to calculate the rest of the data for the corresponding function and parameterised set of Hamiltonians. In the same order as the plots, the chosen values of χ are 110, 140, 110, 150, 70, 90, 70 and 100.

the magnitude of the error terms involved in the algorithm scale as $\mathcal{O}((\Delta t)^3)$. We also make use of a time-splitting method (see Section IV.B.2 in [15]) to improve the numerical accuracy of the algorithm by reducing the amount of time that the MPOs need to be evolved for. Then for each qubit number considered (5, 10, 15, 20, 25, 30, 35 and 40), each parameterised sets of Hamiltonians, and both functions \mathcal{O}_{XZ} and \mathcal{O}_{Sum} , we generate 1000 data samples for training and 250 for testing. The random samples of the inputs are drawn using the same random seed. Thus, for each qubit number, all datasets contains the same input parameters. The values of the functions are then computed using the ITensor Julia library [77] to implement the MPO-based time-splitting algorithm. It should be noted though, that even with the MPO-based algorithm, producing the data in this work required $\sim 10^6$ CPU hours, and thus required access to a supercomputer.

IV. RESULTS

We now report the main numerical results of this study. In Figures 6–13 we show the root mean-squared-error (RMSE), mean absolute error (MAE) and coefficient of determination (R^2) performance metrics for all 6 of the kernels considered and all problem instances. The performance metrics shown on the plots are those for the models with the best hyperparameter values found in the cross-validation (see Appendix B). We show in separate plots the metrics evaluated on training and testing datasets. Tables containing all numerical values plotted in Figures 6–13 (including those not visible on the plots) can be found in Appendix C.

In all Figures 6–13, the linear and cosine kernels are not visible on any of the plots, since they perform so poorly that they never achieve performance metrics within the chosen plot ranges. In contrast, the polynomial and sigmoid kernels perform reasonably well. For a handful of the problem instances, the polynomial and sigmoid kernels achieve R^2 scores on the testing sets exceeding 0.8, and sometimes 0.9, with similar RMSE and MAE values to the Laplacian and RBF kernels. However, all of these kernels are consistently outperformed by the Laplacian and RBF kernels. One can easily see that the performance metrics for the Laplacian and RBF kernels are better on all problem instances considered. For this reason we focus the rest of this sec-

tion on reporting the performance of the Laplacian and RBF kernels, with an emphasis on the testing performance.

In Figures 6 and 7, we can see the performance of the Laplacian and RBF kernels (together with the other kernels) on both the testing and training sets for \mathcal{O}_{XZ} and \mathcal{O}_{Sum} , respectively, with \mathcal{H}_1 . For \mathcal{O}_{XZ} with \mathcal{H}_1 , the Laplacian kernel on the testing set achieves RMSE values between 0.0625 and 0.1137, MAE values from 0.0388 to 0.0763, and R^2 scores ranging from 0.9228 to 0.9696. The RBF kernel, in comparison, shows RMSE values from 0.0837 to 0.1359, MAE values between 0.0431 and 0.0790, and R^2 scores ranging from 0.8771 to 0.9646. For \mathcal{O}_{Sum} with \mathcal{H}_1 , the Laplacian kernel on the testing set yields RMSE values from 0.6176 to 0.8534, MAE values between 0.3579 and 0.5653, and R^2 scores from 0.9429 to 0.9652. While the RBF kernel shows RMSE values from 0.7402 to 1.1179, MAE values between 0.4385 and 0.6916, and R^2 scores ranging from 0.8979 to 0.9556. In both cases, the training performance for both kernels is consistently better than the testing performance, with the Laplacian kernel approaching near-perfect training performance.

Figures 8 and 9 present similar results for \mathcal{O}_{XZ} and \mathcal{O}_{Sum} , respectively, with \mathcal{H}_2 . For \mathcal{O}_{XZ} with \mathcal{H}_2 , the Laplacian kernel on the testing set achieves RMSE values between 0.1100 and 0.1372, MAE values from 0.0709 to 0.0920, and R^2 scores ranging from 0.8452 to 0.8982. Comparatively, the RBF kernel shows RMSE values between 0.0782 and 0.1399, MAE values from 0.0457 to 0.0894, and R^2 scores ranging from 0.8306 to 0.9656. For \mathcal{O}_{Sum} with \mathcal{H}_2 , the Laplacian kernel on the testing set yields RMSE values from 0.8730 to 1.0664, MAE values between 0.5915 and 0.7712, and R^2 scores from 0.8862 to 0.9108. Similarly, the RBF kernel shows RMSE values between 0.6089 and 0.9708, MAE values from 0.3170 to 0.6700, and R^2 scores ranging from 0.8957 to 0.9706. As before, the training performance for both kernels is always superior to the testing performance, but is marginally worse compared with Figures 6 and 7.

Figures 10 and 11 provide results for \mathcal{O}_{XZ} and \mathcal{O}_{Sum} with \mathcal{H}_3 . For \mathcal{O}_{XZ} with \mathcal{H}_3 , the Laplacian kernel on the testing set achieves RMSE values from 0.0670 to 0.0843, MAE values between 0.0424 and 0.0573, and R^2 scores from 0.9537 to 0.9745. The RBF kernel shows comparable RMSE values ranging from 0.0459 to 0.0724, MAE values from 0.0290 to 0.0511, and R^2 scores from 0.9682

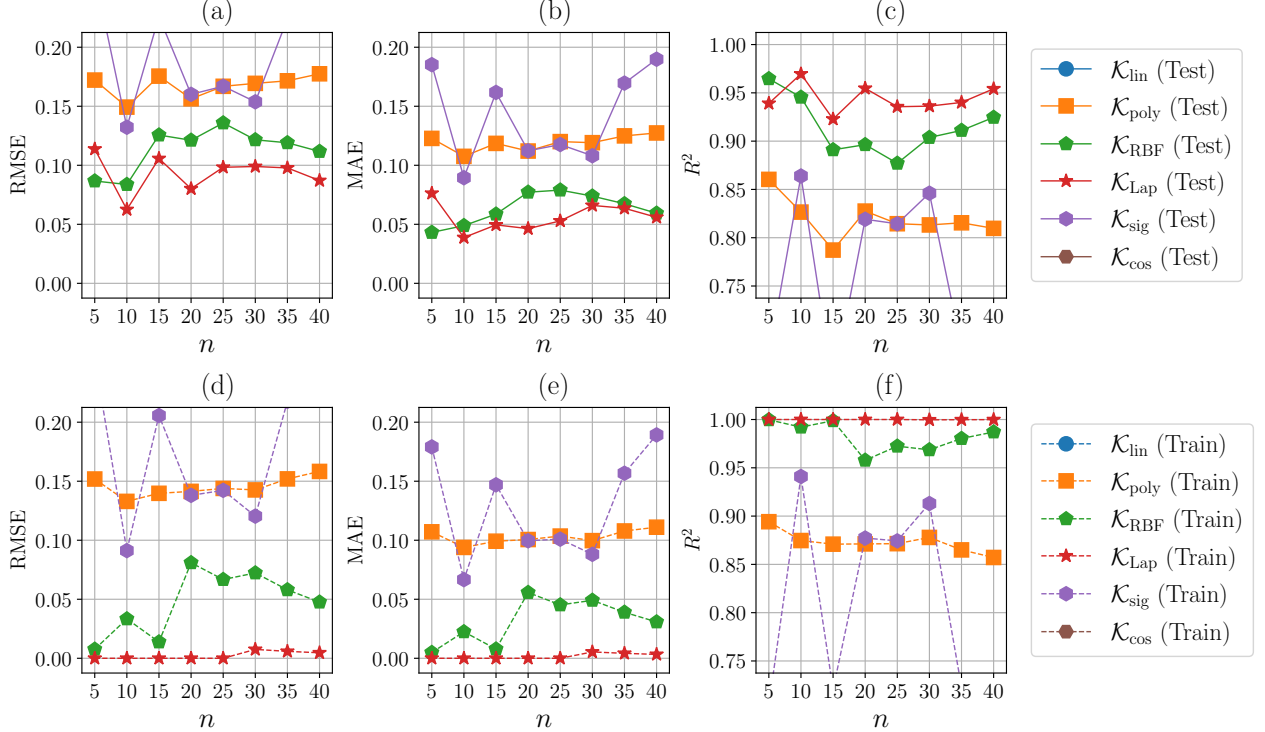


FIG. 6: (\mathcal{O}_{XZ} with \mathcal{K}_1) Learning performance metrics for the best models found in the cross-validation. The metrics are calculated based on predictions made by the models on the testing (Test) and training (Train) sets, with labels determined by \mathcal{O}_{XZ} and \mathcal{K}_1 , for 5-40 qubit systems. The RMSE, MAE and R^2 values are displayed for the testing set in (a)–(c) and the training set in (d)–(f) respectively.

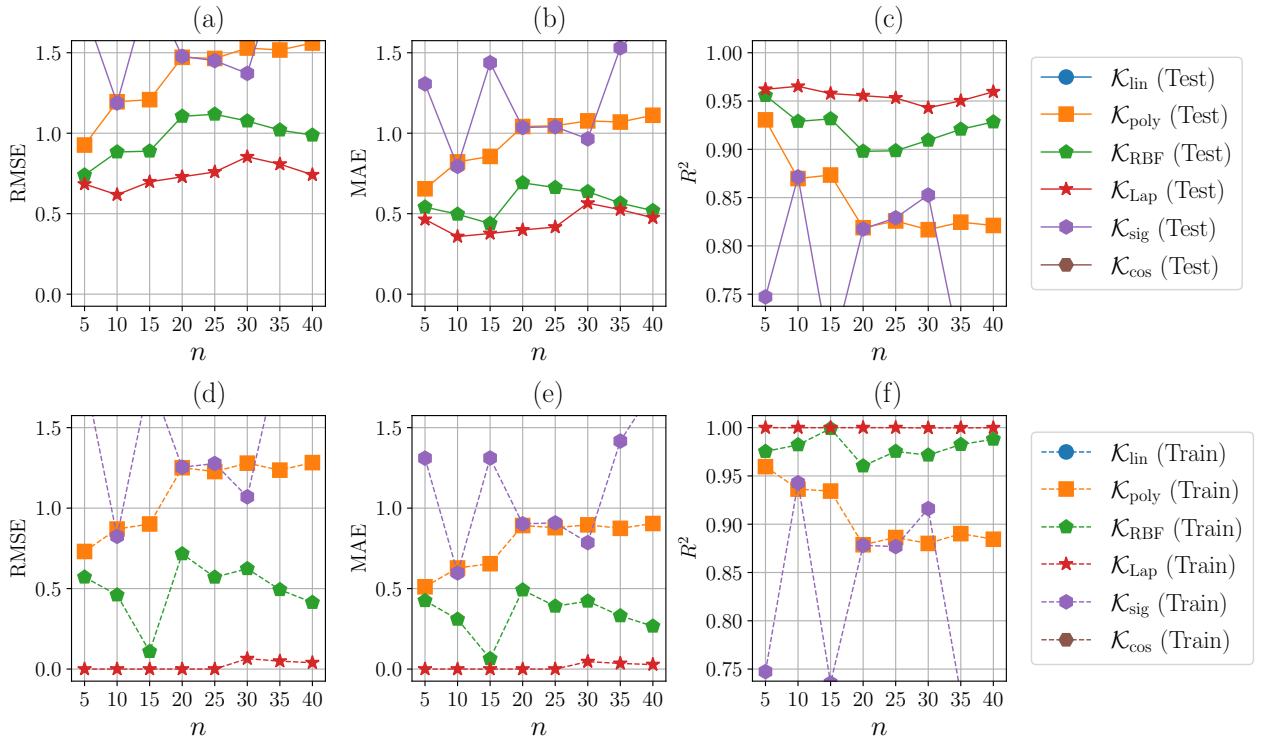


FIG. 7: (\mathcal{O}_{Sum} with \mathcal{K}_1) Learning performance metrics for the best models found in the cross-validation. The metrics are calculated based on predictions made by the models on the testing (Test) and training (Train) sets, with labels determined by \mathcal{O}_{Sum} and \mathcal{K}_1 , for 5-40 qubit systems. The RMSE, MAE and R^2 values are displayed for the testing set in (a)–(c) and the training set in (d)–(f) respectively.

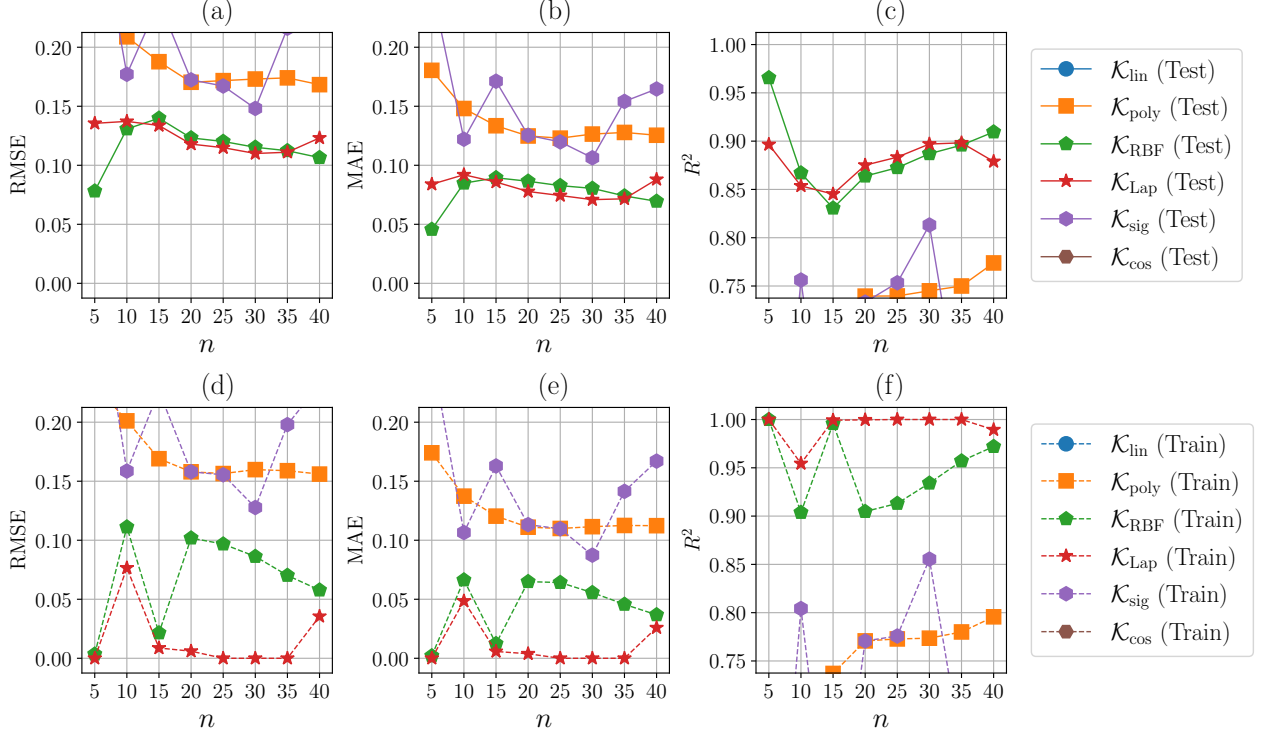


FIG. 8: (\mathcal{O}_{XZ} with \mathcal{H}_2) Learning performance metrics for the best models found in the cross-validation. The metrics are calculated based on predictions made by the models on the testing (Test) and training (Train) sets, with labels determined by \mathcal{O}_{XZ} and \mathcal{H}_2 , for 5-40 qubit systems. The RMSE, MAE and R^2 values are displayed for the testing set in (a)–(c) and the training set in (d)–(f) respectively.

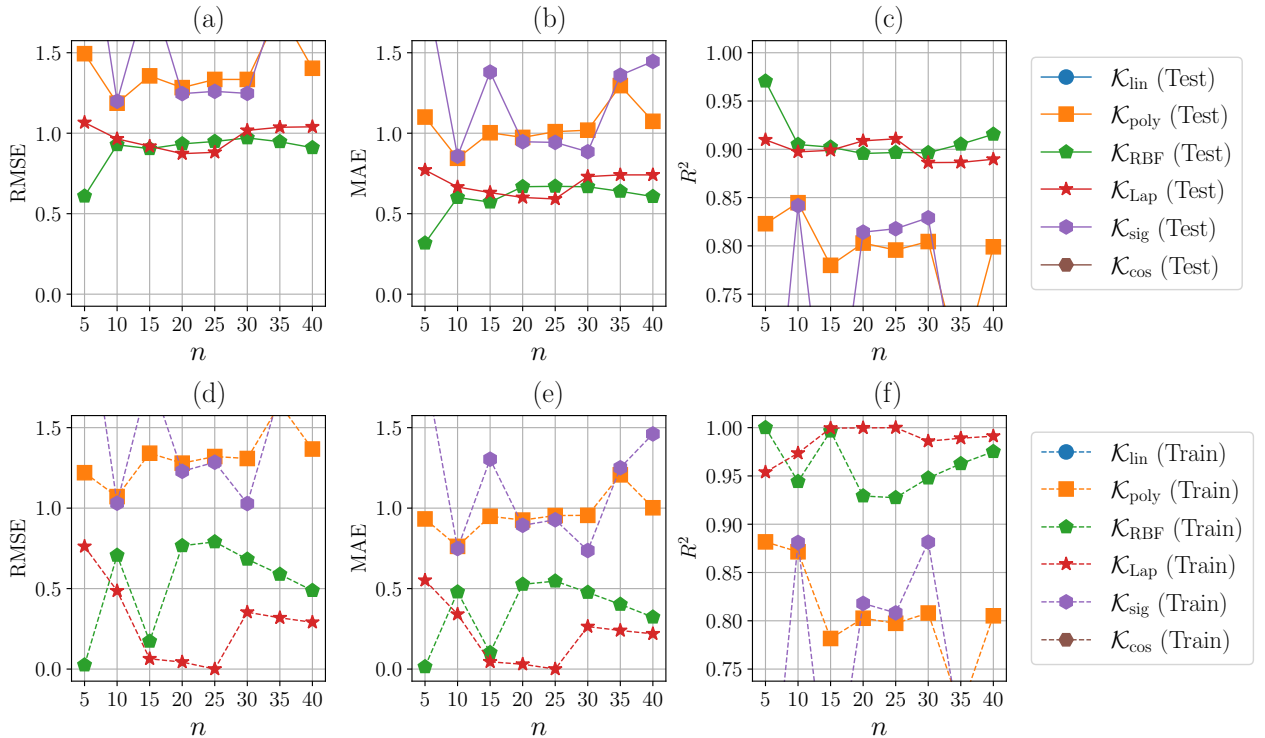


FIG. 9: (\mathcal{O}_{Sum} with \mathcal{H}_2) Learning performance metrics for the best models found in the cross-validation. The metrics are calculated based on predictions made by the models on the testing (Test) and training (Train) sets, with labels determined by \mathcal{O}_{Sum} and \mathcal{H}_2 , for 5-40 qubit systems. The RMSE, MAE and R^2 values are displayed for the testing set in (a)–(c) and the training set in (d)–(f) respectively.

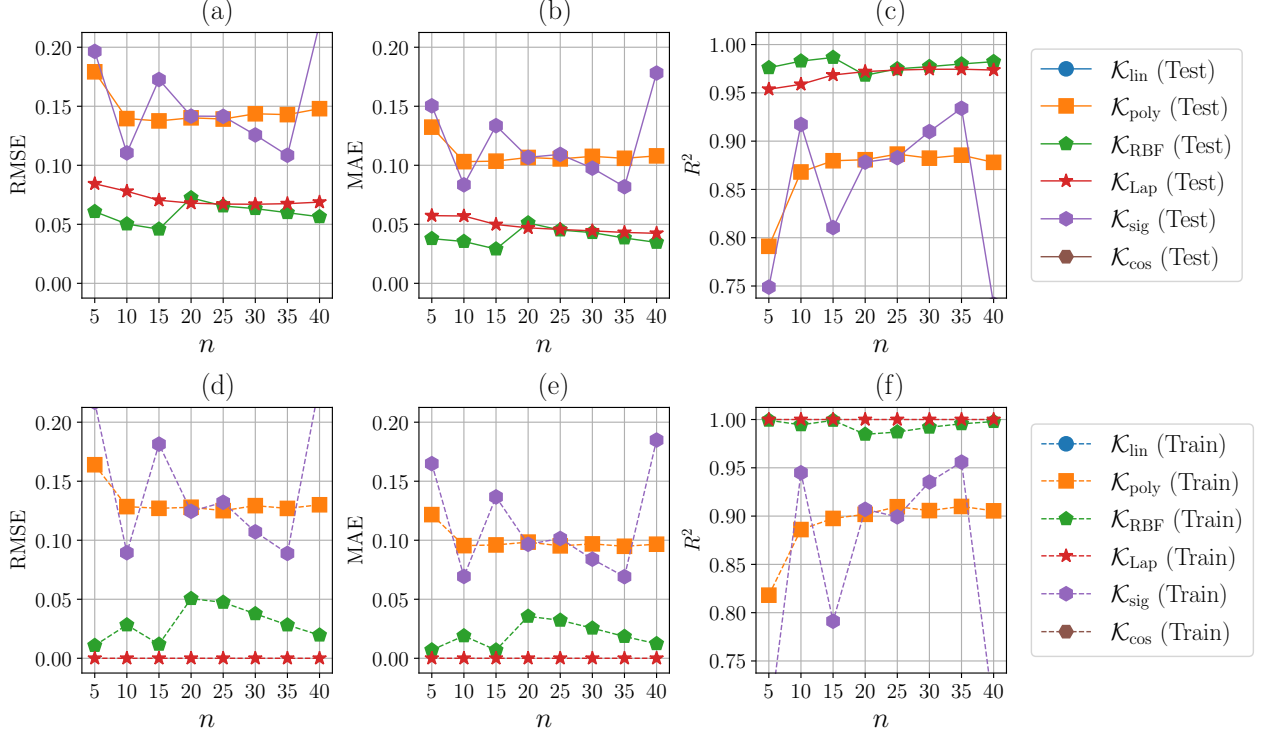


FIG. 10: (\mathcal{O}_{XZ} with \mathcal{K}_3) Learning performance metrics for the best models found in the cross-validation. The metrics are calculated based on predictions made by the models on the testing (Test) and training (Train) sets, with labels determined by \mathcal{O}_{XZ} and \mathcal{K}_3 , for 5-40 qubit systems. The RMSE, MAE and R^2 values are displayed for the testing set in (a)–(c) and the training set in (d)–(f) respectively.

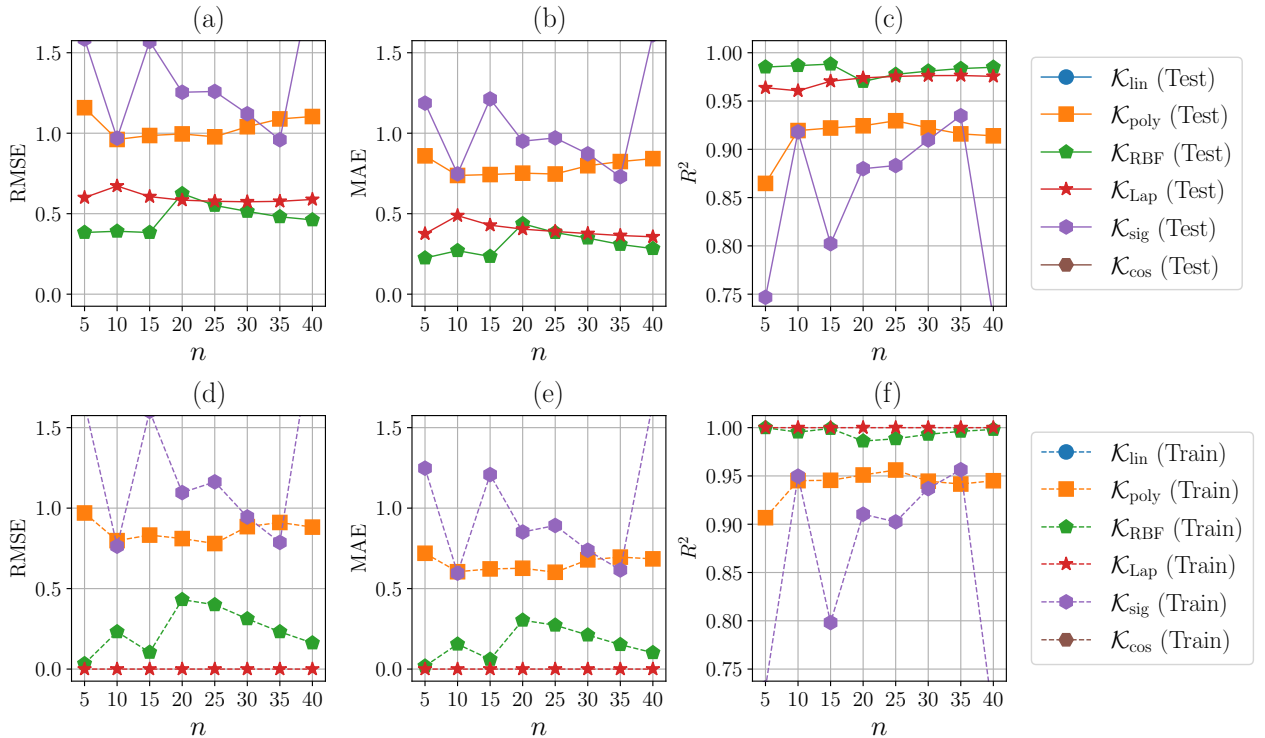


FIG. 11: (\mathcal{O}_{Sum} with \mathcal{K}_3) Learning performance metrics for the best models found in the cross-validation. The metrics are calculated based on predictions made by the models on the testing (Test) and training (Train) sets, with labels determined by \mathcal{O}_{Sum} and \mathcal{K}_3 , for 5-40 qubit systems. The RMSE, MAE and R^2 values are displayed for the testing set in (a)–(c) and the training set in (d)–(f) respectively.

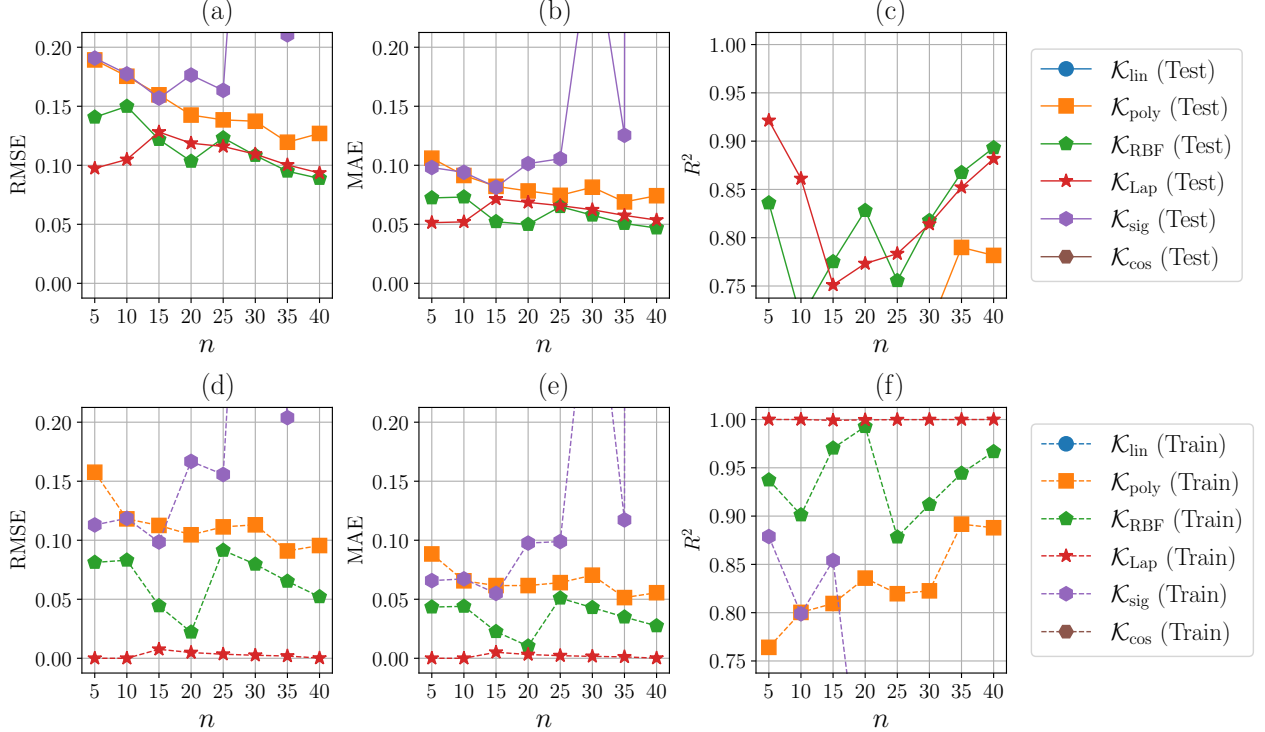


FIG. 12: (\mathcal{O}_{XZ} with \mathcal{H}_4) Learning performance metrics for the best models found in the cross-validation. The metrics are calculated based on predictions made by the models on the testing (Test) and training (Train) sets, with labels determined by \mathcal{O}_{XZ} and \mathcal{H}_4 , for 5-40 qubit systems. The RMSE, MAE and R^2 values are displayed for the testing set in (a)–(c) and the training set in (d)–(f) respectively.

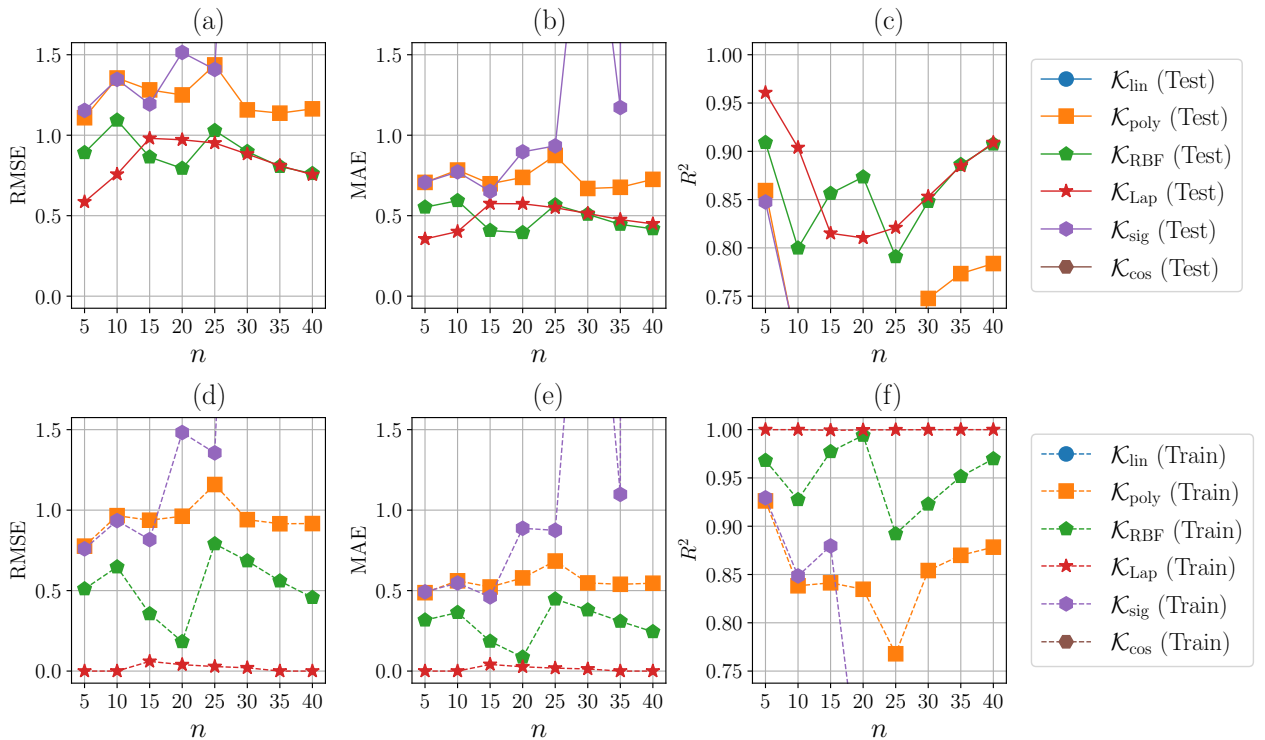


FIG. 13: (\mathcal{O}_{Sum} with \mathcal{H}_4) Learning performance metrics for the best models found in the cross-validation. The metrics are calculated based on predictions made by the models on the testing (Test) and training (Train) sets, with labels determined by \mathcal{O}_{Sum} and \mathcal{H}_4 , for the 5-40 qubit systems. The RMSE, MAE and R^2 values are displayed for the testing set in (a)–(c) and the training set in (d)–(f) respectively.

to 0.9866. For \mathcal{O}_{Sum} with \mathcal{H}_3 , the Laplacian kernel on the testing set yields RMSE values between 0.5740 and 0.6719, MAE values from 0.3564 to 0.4879, and R^2 scores ranging from 0.9606 to 0.9764. Meanwhile the RBF kernel shows RMSE values between 0.3831 and 0.6243, MAE values from 0.2247 to 0.4376, and R^2 scores ranging from 0.9703 to 0.9882. As with previous cases, the training performance for both kernels exceeds their testing performance. However, in these instances the Laplacian kernel exhibits perfect training performance to at least 4 decimal places.

Finally, Figures 12 and 13 show the performance of the kernels on the datasets for \mathcal{O}_{XZ} and \mathcal{O}_{Sum} with \mathcal{H}_4 . For \mathcal{O}_{XZ} with \mathcal{H}_4 , the Laplacian kernel on the testing set achieves RMSE values from 0.0934 to 0.1282, MAE values between 0.0514 and 0.0715, and R^2 scores ranging from 0.7511 to 0.9214. The RBF kernel shows RMSE values from 0.0888 to 0.1499, MAE values between 0.0468 and 0.0731, and R^2 scores from 0.7167 to 0.8931. For \mathcal{O}_{Sum} with \mathcal{H}_4 , the Laplacian kernel yields RMSE values from 0.5859 to 0.9806, MAE values between 0.3555 and 0.5750, and R^2 scores ranging from 0.8103 to 0.9607. While the RBF kernel shows RMSE values from 0.7614 to 1.0930, MAE values between 0.3943 and 0.5934, and R^2 scores from 0.7908 to 0.9091. As in all the other cases, the training performance for both kernels is consistently better than their testing performance, with the Laplacian kernel again achieving almost perfect training performance.

With the exception of a few cases, namely $n = 15, 20$ and 25 in Figure 12, and $n = 10$ and 25 in Figure 13, the R^2 scores on the testing data always exceed 0.8 for both of the Laplacian and RBF kernels, and often exceed 0.9. Similarly, the RMSE and MAE for the Laplacian and RBF kernels on the testing data are small. In the problem instances associated with \mathcal{O}_{XZ} , they almost never exceed 0.15 and are often less than 0.1. In the problem instances associated with \mathcal{O}_{Sum} , they almost never exceed 1.5 and are often less than 1.0. This indicates that the numerical error in the labels predicted by at least one of these kernels for \mathcal{O}_{XZ} , and \mathcal{O}_{Sum} , will generally be smaller than 5–7.5%, and 4–8%, of the range of the functions which returns values in $[-1, 1]$, and $[-3, 9]$, respectively. Note though, that the smallest numerical value of any label determined by \mathcal{O}_{XZ} , and \mathcal{O}_{Sum} , present in the datasets was -0.2297, and -0.1086, respectively.

Overall, the results show that the learning perfor-

mance metrics for the RBF and Laplacian are similar and consistently the best for all problem instances considered. However, while the Laplacian kernel seems to perform better than the RBF kernel in many instances, it also exhibits a larger difference between training and testing performance. This could be interpreted as partial overfitting, which is also supported by observing that the best regularisation strength among those trialled for the Laplacian kernel was frequently $\lambda = 0$ (see Appendix B).

V. DISCUSSION

Our results demonstrate that the Laplacian and RBF kernels can be used to obtain accurate and efficient estimates of OTOCs and related quantities, such as the lower bound in (17). The main cost involved in this approach is that of producing the training dataset. Once we have a trained model, however, it can be used to make predictions for OTOC values instead of continued implementations of the MPO-based algorithm. One could also imagine that if one had access to a fault-tolerant QC, it could be used to supply training data for a ML model. Using KMs, as in this work, would then allow one to obtain an approximation of the correlation landscape in some subset of the Hamiltonian parameter space, without requiring further (potentially expensive) use of the QC. In either case, having the ability to quickly generate approximate predictions of OTOC values for a wide range of Hamiltonians could, for example, assist in identifying interesting behaviours for particular sets of Hamiltonian parameters, which one could then validate by other means.

Given the cost of producing training data, it is natural to ask whether one can obtain similar results with fewer data. To investigate this, we perform a similar procedure as above, but with a varying amount of training data. First, we fix the hyperparameter values for each kernel in each problem instance to be those which were chosen during the cross-validation performed on all of the training data. Next, we choose different training dataset sizes $M \in \mathbb{N}$ to supply to the models. Specifically, for each $M \in \{50m : m = 1, 2, \dots, 20\}$, we randomly sample M of the 1000 training data points, and repeat this 20 times to obtain 20 (possibly intersecting) subsets of size M . We then train a model on each of these 20 subsets of the training data. Finally, we calcu-

late the average R^2 score for the 20 models making predictions on the entire testing set, as an indicator of how the models perform with only M training data samples. The results of this analysis are shown in Figure 14 for the 40-qubit problem instances. The plots show that, even with only a few hundred training data points, the average R^2 scores for the Laplacian and RBF kernels often remain above 0.8, and occasionally reach above 0.9. Thus, the kernels are still capable of learning from fewer training data samples than were supplied in the earlier analysis.

Another point we wish to highlight is that the KM approach allows us to obtain a good approximation of the various OTOC functions (as calculated by the MPO-based algorithm) for systems evolving up to a time linear in the system size. In [54], the authors applied restricted Boltzmann machines to learn OTOCs at early times, which they refer to as the values of t for which $\text{Re}[F(t)] > 0.85$. In contrast, one can infer from Figure 4 that the OTOCs occurring in \mathcal{O}_{Sum} have decayed far below 0.85 (as does the XZ-OTOC). This shows that the KM approach is capable of predicting OTOCs for larger timescales than was achieved in [54].

One limitation of the approach taken here is that the OTOC labels, which were generated using the MPO-based algorithm, are only approximate due to the finite bond dimension. As can be seen in Figure 5, the maximum bond dimension χ selected for producing some of the data would ideally have been larger, especially for the data produced with \mathcal{H}_4 (see Figures 5(d) and 5(h)). However, we did not have the computational resources to increase χ further in these cases. On the other hand, for \mathcal{H}_1 , \mathcal{H}_2 and \mathcal{H}_3 , the values of \mathcal{O}_{XZ} and \mathcal{O}_{Sum} appear to not be changing significantly upon further increase of the bond dimensions above those used to produce the datasets. We also note that the plots in Figure 5 correspond to the 40-qubit systems, which is the largest of the systems used here. For the smaller systems we considered, the convergence with respect to χ will occur more quickly.

Another potential limitation of our ML approach is that one should not expect the kernels to be able to extrapolate beyond the ball in \mathbb{R}^3 from which the parameter values were sampled. Recall, the testing data, on which we evaluated the performance of the models, was drawn from the same distribution as the training data. Thus, what we have demonstrated is that the kernels are able to make accurate predictions for other

Hamiltonians within this region in parameter space. This could nevertheless be useful since this region may contain Hamiltonians which are theoretically interesting but difficult to prepare physically. Indeed, as seen in Figure 4, these regions for different sets of Hamiltonians are sufficiently large to capture a qualitatively rich variety of behaviours in the underlying quantum systems.

VI. CONCLUSION

In this paper, we explored the application of classical KMs to learn and predict the OTOC, an important quantity used to investigate quantum information scrambling. By viewing the XZ-OTOC, and the sum of OTOCs in (17), as functions of parameters associated with a parameterised set of Hamiltonians, we frame the learning task as a regression problem and employ 6 standard kernel functions. For all 4 of the parameterised sets of Hamiltonians considered, the results show that the Laplacian and RBF kernels perform best. They are both capable of closely approximating the XZ-OTOC and the sum of OTOCs (as calculated by the MPO-based algorithm) from a moderate amount of training data. Even for systems with reasonably large qubit numbers, the Laplacian and RBF kernels often achieve R^2 scores on the testing data between 0.9 and 0.99, and almost always at least 0.8, accompanied by small values for the RMSE and MAE.

With these trained kernels, it is possible to efficiently investigate the behaviour of the OTOC across a wide range of systems. Of course, obtaining the trained kernels required significant computational costs to produce training data. However, we have shown here that it is possible to obtain a sufficient amount of data to accurately learn the OTOC functions that we considered. Indeed, we saw that KMs can achieve good learning performance metrics (e.g., $R^2 > 0.8$) from a few hundred data points. The value of the KM approach, therefore, is in situations where one would like to know the behaviour of the OTOCs across a much larger number of systems ($\gtrsim 10^3$) within the parameterised sets. The KMs can efficiently predict the values for all of these systems from a few hundred data points, which is a comparatively much smaller cost than simulating each of these systems individually.

Our work improves on aspects of previous work [54]

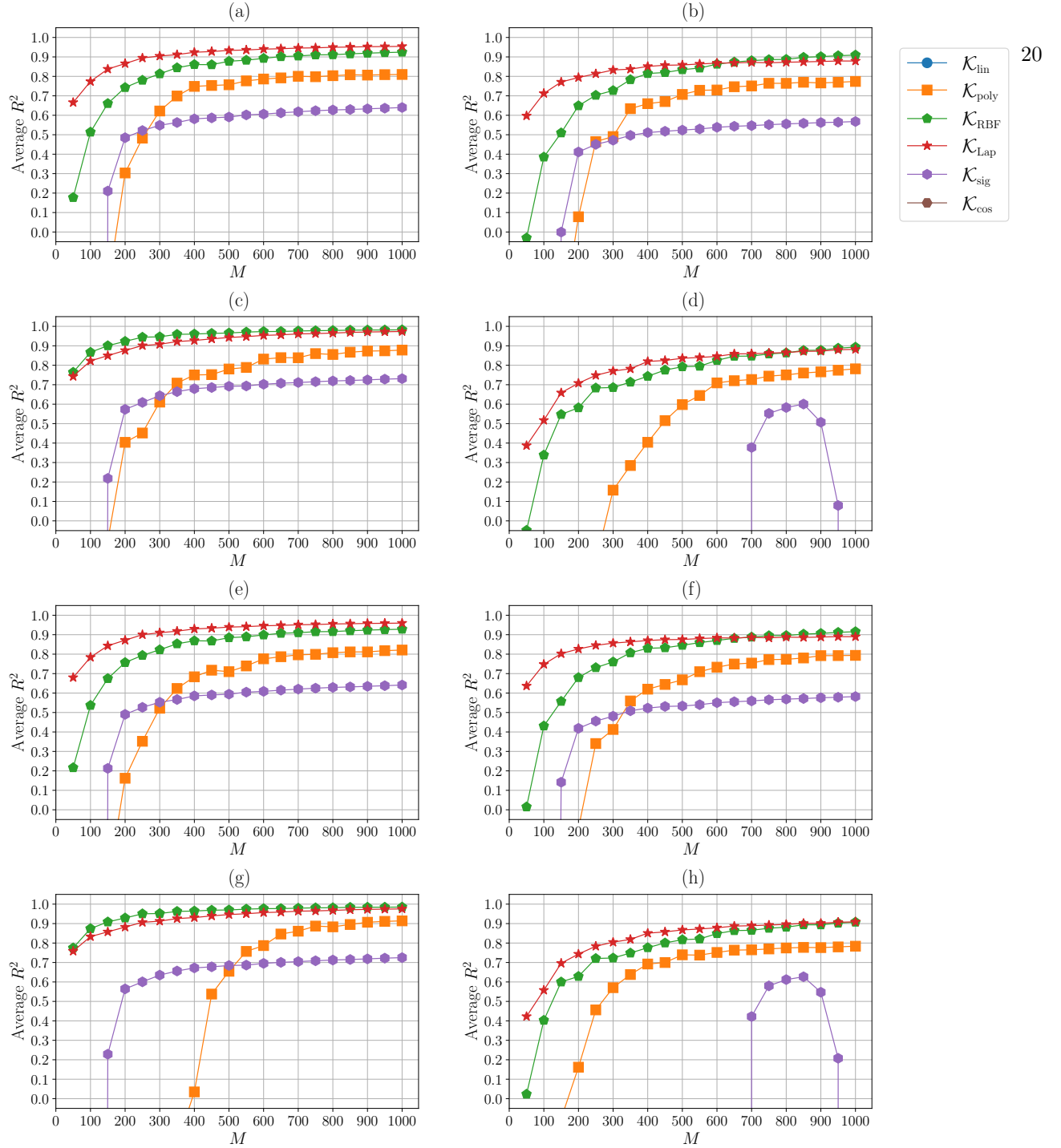


FIG. 14: Average coefficient of determination R^2 for each kernel making predictions on the 40-qubit testing sets, plotted against the number of training data samples M used to train the associated ML models. Each point in the plots corresponds to the numerical value of R^2 averaged over 20 different models using the same kernel. Each of the models is the result of applying Algorithm 1 with a random subset of the training data containing M of the total 1000 training data samples. The hyperparameters are fixed to be the best hyperparameters found during the 10-fold cross-validation performed on all 1000 training data samples. Plots (a), (b), (c) and (d) show the average R^2 score on the testing datasets with labels determined by \mathcal{O}_{XZ} with \mathcal{H}_1 , \mathcal{H}_2 , \mathcal{H}_3 and \mathcal{H}_4 , respectively. Plots (e), (f), (g) and (h) show the average R^2 score on the testing datasets with labels determined by \mathcal{O}_{Sum} with \mathcal{H}_1 , \mathcal{H}_2 , \mathcal{H}_3 and \mathcal{H}_4 , respectively.

which used ML to approximate OTOCs for early times. Here we derive ML models which can make accurate predictions over timescales which are linear in the size of the underlying quantum system, exceeding the early timescales considered in [54]. We also provide a significant body of numerical evidence showing that the KM approach works well for many instances of the problem. Nonetheless, one should not expect that the KM approach will allow us to predict OTOCs and related functions for arbitrary inputs, but only for those sampled from the same subset as the input training data. However, this can still be useful since the domains of the learned models are sufficiently large to describe a diverse spectrum of behaviours in a quantum system.

The paper naturally lends itself to a handful of possible extensions, which we suggest as future research directions. For example, one may like to investigate whether the KM approach works with other OTOCs, other linear combinations of OTOCs, or other types of correlation functions such as the Loschmidt echo [78]. We could also examine how the approach works for different or larger parameterised sets of Hamiltonians. For instance, we could investigate sets with $d > 3$ (i.e., parameterised by 4 or more parameters), sets containing Hamiltonians describing quantum systems in higher dimensions, or sets containing highly non-local Pauli strings in one or more terms. Though producing data for the latter two cases would likely be challenging. Similarly, it might be interesting to apply quantum kernel methods [79–81] to investigate whether a problem-specific quantum kernel may offer significant increases in learning performance. Finally, it could be useful to explore how the results change in response to larger values of χ in the MPO calculations, and increases in the size of the region from which we sample the input data.

ACKNOWLEDGMENTS

The authors thank Jason Twamley for insightful conversations on the out-of-time ordered correlator, which inspired the initial concept of this study. The authors would also like to thank Lyle Noakes and Yusen Wu for invaluable discussions. JT is supported by an Australian Government Research Training Program (RTP) Scholarship. JP was supported by the Brian Dunlop Physics Fellowship at The University of Western Australia and is supported at Nordita by the Wenner-Gren Foundations and, in part, by the Wallenberg Initiative on Networks and Quantum Information (WINQ). Nordita is supported in part by NordForsk. This work was supported by resources provided by the Pawsey Supercomputing Research Centre with funding from the Australian Government and the Government of Western Australia.

DATA AVAILABILITY

The datasets produced in this study are available in the GitHub repository at <https://github.com/John-J-Tanner/ITensor-OTOC-Data>. The repository includes all relevant datasets necessary to replicate the study’s results. For further information or inquiries, please contact the corresponding author, John Tanner, at john.tanner@uwa.edu.au.

[1] L. S. Madsen, F. Laudenbach, M. F. Askarani, F. Rortais, T. Vincent, J. F. F. Bulmer, F. M. Miatto, L. Neuhaus, L. G. Helt, and M. J. Collins et al. Quantum computational advantage with a programmable photonic processor. *Nature* **606**, 75–81 (2022).

[2] C. D. Bruzewicz, J. Chiaverini, R. McConnell, and J. M. Sage. Trapped-ion quantum computing: Progress and challenges. *Appl. Phys. Rev.* **6**, 021314 (2019).

[3] S. J. Evered, D. Bluvstein, M. Kalinowski, S. Ebadi, T. Manovitz, H. Zhou, S. H. Li, A. A. Geim, T. T. Wang, and N. Maskara et al. High-fidelity parallel entangling gates on a neutral-atom quantum computer. *Nature* **622**, 268–272 (2023).

[4] T. E. O’Brien, L. B. Ioffe, Y. Su, D. Fushman, H. Neven, R. Babbush, and V. Smelyanskiy. Quantum computation of molecular structure using data from challenging-to-classically-simulate nuclear magnetic resonance experiments. *PRX Quantum* **3**, 030345 (2022).

[5] S. Bravyi, O. Dial, J. M. Gambetta, D. Gil, and Z. Nazario. The future of quantum computing with superconducting qubits. *J. Appl. Phys.* **132**, 160902 (2022).

[6] K. A. Landsman, C. Figgatt, T. Schuster, N. M. Linke, B. Yoshida, N. Y. Yao, and C. Monroe. Verified quantum information scrambling. *Nature* **567**, 61–65 (2019).

[7] P. Hayden and J. Preskill. Black holes as mirrors: quantum information in random subsystems. *J. High Energ. Phys.* **2007**, 120 (2007).

[8] Y. Sekino and L. Susskind. Fast scramblers. *J. High Energ. Phys.* **2008**, 65 (2008).

[9] S. H. Shenker and D. Stanford. Black holes and the butterfly effect. *J. High Energ. Phys.* **2014**, 67 (2014).

[10] S. H. Shenker and D. Stanford. Stringy effects in scrambling. *J. High Energ. Phys.* **2015**, 132 (2015).

[11] P. Richerme, Z. X. Gong, A. Lee, C. Senko, J. Smith, M. Foss-Feig, S. Michalakis, A. V. Gorshkov, and C. Monroe. Non-local propagation of correlations in quantum systems with long-range interactions. *Nature* **511**, 198–201 (2014).

[12] P. Jurcevic, B. P. Lanyon, P. Hauke, C. Hempel, P. Zoller, R. Blatt, and C. F. Roos. Quasiparticle engineering and entanglement propagation in a quantum many-body system. *Nature* **511**, 202–205 (2014).

[13] R. J. Lewis-Swan, A. Safavi-Naini, A. M. Kaufman, and A. M. Rey. Dynamics of quantum information. *Nat. Rev. Phys.* **1**, 627–634 (2019).

[14] K. Hashimoto, K. Murata, and R. Yoshii. Out-of-time-order correlators in quantum mechanics. *J. High Energ. Phys.* **2017**, 138 (2017).

[15] S. Xu and B. Swingle. Scrambling dynamics and out-of-time ordered correlators in quantum many-body systems: a tutorial. *PRX Quantum* **5**, 010201 (2024).

[16] A. I. Larkin and Y. N. Ovchinnikov. Quasiclassical method in the theory of superconductivity. *Sov. Phys. JETP* **28**, 1200 (1969).

[17] E. H. Lieb and D. W. Robinson. The finite group velocity of quantum spin systems. *Commun. Math. Phys.* **28**, 251–257 (1972).

[18] D. A. Roberts and B. Swingle. Lieb-robinson bound and the butterfly effect in quantum field theories. *Phys. Rev. Lett.* **117**, 091602 (2016).

[19] Y. Huang, Y.-L. Zhang, and X. Chen. Out-of-time-ordered correlators in many-body localized systems. *Annalen Der Physik* **529(7)**, 1600318 (2017).

[20] X. Chen, T. Zhou, D. A. Huse, and E. Fradkin. Out-of-time-order correlations in many-body localized and thermal phases. *Annalen Der Physik* **529(7)**, 1600332 (2017).

[21] M. C. Bañuls, N. Y. Yao, S. Choi, M. D. Lukin, and J. I. Cirac. Dynamics of quantum information in many-body localized systems. *Phys. Rev. B* **96**, 174201 (2017).

[22] D.-L. Deng, X. Li, J. H. Pixley, Y.-L. Wu, and S. D. Sarma. Logarithmic entanglement lightcone in many-body localized systems. *Phys. Rev. B* **95**, 024202 (2017).

[23] K. Slagle, Z. Bi, Y.-Z. You, and C. Xu. Out-of-time-order correlation in marginal many-body localized systems. *Phys. Rev. B* **95**, 165136 (2017).

[24] P. Hosur, X.-L. Qi, D. A. Roberts, and B. Yoshida. Chaos in quantum channels. *J. High Energ. Phys.* **2016**, 4 (2016).

[25] E. B. Rozenbaum, S. Ganeshan, and V. Galitski. Lyapunov exponent and out-of-time-ordered correlator’s growth rate in a chaotic system. *Phys. Rev. Lett.* **118**, 086801 (2017).

[26] I. García-Mata, R. Jalabert, and D. Wisniacki. Out-of-time-order correlations and quantum chaos. *Scholarpedia*, **18(4):55237** (2023).

[27] S. F. E. Oliviero, L. Leone, S. Lloyd, and A. Hamma. Unscrambling quantum information with clifford decoders. *Phys. Rev. Lett.* **132**, 080402 (2024).

[28] B. Swingle. Unscrambling the physics of out-of-time-order correlators. *Nature Phys.* **14**, 988–990 (2018).

[29] V. Balachandran, G. Benenti, G. Casati, and D. Pöletti. From the eigenstate thermalization hypothesis to algebraic relaxation of otocs in systems with conserved quantities. *Phys. Rev. B* **104**, 104306 (2021).

[30] D. Yuan, S.-Y. Zhang, Y. Wang, L.-M. Duan, and D.-L. Deng. Quantum information scrambling in quantum many-body scarred systems. *Phys. Rev. Research* **4**,

023095 (2022).

[31] J. Maldacena, S. H. Shenker, and D. Stanford. A bound on chaos. *J. High Energ. Phys.* **2016**, *106* (2016).

[32] H. Gharibyan, M. Hanada, B. Swingle, and M. Tezuka. Quantum lyapunov spectrum. *J. High Energ. Phys.* **2019**, *82* (2019).

[33] N. Dowling, P. Kos, and K. Modi. Scrambling is necessary but not sufficient for chaos. *Phys. Rev. Lett.* **131**, *180403* (2023).

[34] T. Schuster, M. Niu, J. Cotler, T. O'Brien, J. R. McClean, and M. Mohseni. Learning quantum systems via out-of-time-order correlators. *Phys. Rev. Research* **5**, *043284* (2023).

[35] J. Cotler, T. Schuster, and M. Mohseni. Information-theoretic hardness of out-of-time-order correlators. *Phys. Rev. A* **108**, *062608* (2023).

[36] J. Polchinski and V. Rosenhaus. The spectrum in the sachdev-ye-kitaev model. *J. High Energ. Phys.* **2016**, *1* (2016).

[37] J. Maldacena and D. Stanford. Remarks on the sachdev-ye-kitaev model. *Phys. Rev. D* **94**, *106002* (2016).

[38] C.-J. Lin and O. I. Motrunich. Out-of-time-ordered correlators in a quantum ising chain. *Phys. Rev. B* **97**, *144304* (2018).

[39] M. McGinley, A. Nunnenkamp, and J. Knolle. Slow growth of out-of-time-order correlators and entanglement entropy in integrable disordered systems. *Phys. Rev. Lett.* **122**, *020603* (2019).

[40] M. Heyl, F. Pollmann, and B. Dóra. Detecting equilibrium and dynamical quantum phase transitions in ising chains via out-of-time-ordered correlators. *Phys. Rev. Lett.* **121**, *016801* (2018).

[41] S. Xu and B. Swingle. Accessing scrambling using matrix product operators. *Nat. Phys.* **16**, *199–204* (2020).

[42] S. Paeckel, T. Köhler, A. Swoboda, S. R. Manmana, U. Schollwöck, and C. Hubig. Time-evolution methods for matrix-product states. *Annals of Physics* **411**, *167998* (2019).

[43] N. Schuch, M. M. Wolf, F. Verstraete, and J. I. Cirac. Computational complexity of projected entangled pair states. *Phys. Rev. Lett.* **98**, *140506* (2007).

[44] A. Garcia-Saez and J. I. Latorre. An exact tensor network for the 3sat problem. *Quantum Inf. Comput.* **12**, *0283* (2012).

[45] B. Swingle, G. Bentsen, M. Schleier-Smith, and P. Hayden. Measuring the scrambling of quantum information. *Phys. Rev. A* **94**, *040302(R)* (2016).

[46] M. Gärttner, J. G. Bohnet, A. Safavi-Naini, M. J. Wall, J. J. Bollinger, and A. M. Rey. Measuring out-of-time-order correlations and multiple quantum spectra in a trapped-ion quantum magnet. *Nat. Phys.* **13**, *781–786* (2017).

[47] J. Li, R. Fan, H. Wang, B. Ye, B. Zeng, H. Zhai, X. Peng, and J. Du. Measuring out-of-time-order correlators on a nuclear magnetic resonance quantum simulator. *Phys. Rev. X* **7**, *031011* (2017).

[48] S. Pg, N. D. Varikuti, and V. Madhok. Exponential speedup in measuring out-of-time-ordered correlators and gate fidelity with a single bit of quantum information. *Physics Letters A* **397** (2021) *127257*.

[49] P. D. Blocher, S. Asaad, V. Mourik, M. A. I. Johnson, A. Morello, and K. Mølmer. Measuring out-of-time-ordered correlation functions without reversing time evolution. *Phys. Rev. A* **106**, *042429* (2022).

[50] J. Preskill. Quantum computing in the nisq era and beyond. DOI: [Quantum 2, 79](https://doi.org/10.22331/q-2018-08-09-79) (2018).

[51] I. Steinwart and A. Christmann. *Support Vector Machines*. Springer, 2008.

[52] B. Schölkopf and A. J. Smola. *Learning with Kernels: Support Vector Machines, Regularization, Optimization, and Beyond*. MIT Press, Cambridge, MA, USA, 2001.

[53] M. Mohri, A. Rostamizadeh, and A. Talwalkar. *Foundations of Machine Learning*. MIT Press, Cambridge, MA, USA, 2018.

[54] Y. Wu, L.-M. Duan, and D.-L. Deng. Artificial neural network based computation for out-of-time-ordered correlators. *Phys. Rev. B* **101**, *214308* (2020).

[55] V. N. Vapnik. *Statistical Learning Theory*. Wiley-Interscience, 1998.

[56] R. Penrose. A generalized inverse for matrices. *Mathematical Proceedings of the Cambridge Philosophical Society.* **51**(3):406-413 (1955).

[57] A. W. Harrow, L. Kong, Z.-W. Liu, and P. Shor. Separation of out-of-time-ordered correlation and entanglement. *PRX Quantum* **2**, *020339* (2021).

[58] Mark Wilde. *Quantum information theory*. Cambridge University Press, 2013.

[59] M. Nielsen and I. Chuang. *Quantum Computation and Quantum Information*. Cambridge University Press, 2000.

[60] B. Yoshida and A. Kitaev. Efficient decoding for the hayden-preskill protocol. [arXiv:1710.03363](https://arxiv.org/abs/1710.03363).

[61] I. Cong, S. Choi, and M. D. Lukin. Quantum convolutional neural networks. *Nat. Phys.* **15**, *1273–1278* (2019).

[62] Y. Wu, B. Wu, J. Wang, and X. Yuan. Quantum phase recognition via quantum kernel methods. *Quantum* **7**, *981* (2023).

[63] L. A. Takhtadzhan and L. D. Faddeev. The quantum method of the inverse problem and the heisenberg xyz model. *Russ. Math. Surv.* **34**, *11* (1979).

[64] F. Pinheiro, G. M. Bruun, J.-P. Martikainen, and J. Larson. Xyz quantum heisenberg models with p-orbital bosons. *Phys. Rev. Lett.* **111**, *205302* (2013).

[65] R. Rota, F. Minganti, A. Biella, and C. Ciuti. Dynamical properties of dissipative xyz heisenberg lattices. *New J. Phys.* **20**, 045003 (2018).

[66] A.-B.A. Mohamed, A.-H. Abdel-Aty, E. G. El-Hadidy, and H. A.A. El-Saka. Two-qubit heisenberg xyz dynamics of local quantum fisher information, skew information coherence: Dyzaloshinskii–moriya interaction and decoherence. *Results in Physics* **30**, 104777 (2021).

[67] C. K. Majumdar and D. K. Ghosh. On next-nearest-neighbor interaction in linear chain. i. *J. Math. Phys.* **10**, 1388–1398 (1969).

[68] C. K. Majumdar and D. K. Ghosh. On next-nearest-neighbor interaction in linear chain. ii. *J. Math. Phys.* **10**, 1399–1402 (1969).

[69] W. J. Caspers, K. M. Emmett, and W. Magnus. The majumdar-ghosh chain. twofold ground state and elementary excitations. *J. Phys. A: Math. Gen.* **17**, 2687 (1984).

[70] R. W. Chhajlany, P. Tomczak, A. Wójcik, and J. Richter. Entanglement in the majumdar-ghosh model. *Phys. Rev. A* **75**, 032340 (2007).

[71] X. M. Weng and Z. Y. Li. Transverse-random-field mixed ising model with arbitrary spins. *Phys. Rev. B* **53**, 12142 (1996).

[72] J. Wurtz and A. Polkovnikov. Emergent conservation laws and nonthermal states in the mixed-field ising model. DOI: *Phys. Rev. B* **101**, 195138 (2020).

[73] Y. Chiba. Proof of absence of local conserved quantities in the mixed-field ising chain. *Phys. Rev. B* **109**, 035123 (2024).

[74] F. Pedregosa, G. Varoquaux, A. Gramfort, V. Michel, B. Thirion, O. Grisel, M. Blondel, P. Prettenhofer, R. Weiss, and V. Dubourg et al. Scikit-learn: Machine learning in Python. *JMLR* **12**(85), 2825–2830 (2011).

[75] G. Vidal. Efficient classical simulation of slightly entangled quantum computations. *Phys. Rev. Lett.* **91**, 147902 (2003).

[76] G. Vidal. Efficient simulation of one-dimensional quantum many-body systems. *Phys. Rev. Lett.* **93**, 040502 (2004).

[77] M. Fishman, S. R. White, and E. M. Stoudenmire. The itensor software library for tensor network calculations. *SciPost Phys. Codebases* **4** (2022).

[78] A. Goussev, R. A. Jalabert, H. M. Pastawski, and D. Wisniacki. Loschmidt echo. *Scholarpedia*, **7**(8):11687 (2012).

[79] M. Schuld and F. Petruccione. *Quantum Models as Kernel Methods*, pages 217–245. Springer International Publishing, 2021. DOI: [10.1007/978-3-030-83098-4_6](https://doi.org/10.1007/978-3-030-83098-4_6).

[80] Y. Liu, S. Arunachalam, and K. Temme. A rigorous and robust quantum speed-up in supervised machine learning. *Nat. Phys.* **17**, 1013–1017 (2021).

[81] V. Havlíček, A. D. Cárcoles, K. Temme, A. W. Harrow, A. Kandala, J. M. Chow, and J. M. Gambetta. Supervised learning with quantum-enhanced feature spaces. *Nature* **567**, 209–212 (2019).

[82] G. H. Golub and C. F. Van Loan. *Matrix Computations*. Johns Hopkins University Press, 4th edition, 2013.

Appendix A: Supplementary results

Theorem A.1. Let $\mathcal{X} \equiv \mathbb{R}^d$ be the input data domain and $\mathcal{D} = \{(\mathbf{x}_i, y_i)\}_{i=1}^M \subseteq \mathcal{X} \times \mathbb{R}$ be a training dataset. Let $\mathcal{K} : \mathcal{X} \times \mathcal{X} \rightarrow \mathbb{R}$ be a kernel and define $\tilde{\mathcal{L}}_{\mathcal{D}} : \mathbb{R}^M \rightarrow \mathbb{R}$ s.t.

$$\tilde{\mathcal{L}}_{\mathcal{D}}(\vec{\alpha}) = \frac{1}{M} \|K\vec{\alpha} - \vec{y}\|^2 + \frac{\lambda}{M} \langle \vec{\alpha}, K\vec{\alpha} \rangle \quad (\text{A1})$$

where $\|\cdot\|$ is the Euclidean norm, $\langle \cdot, \cdot \rangle$ is the Euclidean inner product, $\vec{y} = (y_i)_{i=1}^M \in \mathbb{R}^M$ is the vector of training

data labels, $K_{ij} = \mathcal{K}(\mathbf{x}_i, \mathbf{x}_j)$ is the kernel matrix for the input training data $\{\mathbf{x}_i\}_{i=1}^M$. Then (A1) defines a smooth convex map.

Proof. The map $\tilde{\mathcal{L}}_{\mathcal{D}}$ is clearly smooth since it is just a polynomial in the components of $\vec{\alpha}$. In order to show that $\tilde{\mathcal{L}}_{\mathcal{D}}$ is convex we need to show that

$$\tilde{\mathcal{L}}_{\mathcal{D}}(\mu\vec{\alpha}_1 + (1-\mu)\vec{\alpha}_2) \leq \mu\tilde{\mathcal{L}}_{\mathcal{D}}(\vec{\alpha}_1) + (1-\mu)\tilde{\mathcal{L}}_{\mathcal{D}}(\vec{\alpha}_2) \quad (\text{A2})$$

for all $\vec{\alpha}_1, \vec{\alpha}_2 \in \mathbb{R}^M$ and $\mu \in [0, 1]$. So let $\vec{\alpha}_1, \vec{\alpha}_2 \in \mathbb{R}^M$ and $\mu \in [0, 1]$ then

$$\begin{aligned} & \tilde{\mathcal{L}}_{\mathcal{D}}(\mu\vec{\alpha}_1 + (1-\mu)\vec{\alpha}_2) \\ &= \frac{1}{M} \|K(\mu\vec{\alpha}_1 + (1-\mu)\vec{\alpha}_2) - \vec{y}\|^2 + \frac{\lambda}{M} \langle \mu\vec{\alpha}_1 + (1-\mu)\vec{\alpha}_2, K(\mu\vec{\alpha}_1 + (1-\mu)\vec{\alpha}_2) \rangle \\ &= \frac{1}{M} \|\mu(K\vec{\alpha}_1 - \vec{y}) + (1-\mu)(K\vec{\alpha}_2 - \vec{y})\|^2 + \frac{\lambda}{M} \langle \mu\vec{\alpha}_1 + (1-\mu)\vec{\alpha}_2, K(\mu\vec{\alpha}_1 + (1-\mu)\vec{\alpha}_2) \rangle. \\ &= \frac{1}{M} \left(\mu^2 \|K\vec{\alpha}_1 - \vec{y}\|^2 + 2\mu(1-\mu) \langle K\vec{\alpha}_1 - \vec{y}, K\vec{\alpha}_2 - \vec{y} \rangle + (1-\mu)^2 \|K\vec{\alpha}_2 - \vec{y}\|^2 \right) \\ &\quad + \frac{\lambda}{M} \left(\mu^2 \langle \vec{\alpha}_1, K\vec{\alpha}_1 \rangle + 2\mu(1-\mu) \langle \vec{\alpha}_1, K\vec{\alpha}_2 \rangle + (1-\mu)^2 \langle \vec{\alpha}_2, K\vec{\alpha}_2 \rangle \right). \\ &= \frac{1}{M} \left((-\mu(1-\mu) + \mu) \|K\vec{\alpha}_1 - \vec{y}\|^2 + 2\mu(1-\mu) \langle K\vec{\alpha}_1 - \vec{y}, K\vec{\alpha}_2 - \vec{y} \rangle + (-\mu(1-\mu) + (1-\mu)) \|K\vec{\alpha}_2 - \vec{y}\|^2 \right) \\ &\quad + \frac{\lambda}{M} \left((-\mu(1-\mu) + \mu) \langle \vec{\alpha}_1, K\vec{\alpha}_1 \rangle + 2\mu(1-\mu) \langle \vec{\alpha}_1, K\vec{\alpha}_2 \rangle + (-\mu(1-\mu) + (1-\mu)) \langle \vec{\alpha}_2, K\vec{\alpha}_2 \rangle \right). \\ &= \frac{1}{M} \left(\mu \|K\vec{\alpha}_1 - \vec{y}\|^2 + (1-\mu) \|K\vec{\alpha}_2 - \vec{y}\|^2 - \mu(1-\mu) \|(K\vec{\alpha}_1 - \vec{y}) - (K\vec{\alpha}_2 - \vec{y})\|^2 \right) \\ &\quad + \frac{\lambda}{M} \left(\mu \langle \vec{\alpha}_1, K\vec{\alpha}_1 \rangle + (1-\mu) \langle \vec{\alpha}_2, K\vec{\alpha}_2 \rangle - \mu(1-\mu) \langle \vec{\alpha}_1 - \vec{\alpha}_2, K(\vec{\alpha}_1 - \vec{\alpha}_2) \rangle \right). \\ &\leq \frac{1}{M} \left(\mu \|K\vec{\alpha}_1 - \vec{y}\|^2 + (1-\mu) \|K\vec{\alpha}_2 - \vec{y}\|^2 \right) + \frac{\lambda}{M} \left(\mu \langle \vec{\alpha}_1, K\vec{\alpha}_1 \rangle + (1-\mu) \langle \vec{\alpha}_2, K\vec{\alpha}_2 \rangle \right). \\ &= \mu\tilde{\mathcal{L}}_{\mathcal{D}}(\vec{\alpha}_1) + (1-\mu)\tilde{\mathcal{L}}_{\mathcal{D}}(\vec{\alpha}_2). \end{aligned} \quad (\text{A3})$$

Hence $\tilde{\mathcal{L}}_{\mathcal{D}}(\mu\vec{\alpha}_1 + (1-\mu)\vec{\alpha}_2) \leq \mu\tilde{\mathcal{L}}_{\mathcal{D}}(\vec{\alpha}_1) + (1-\mu)\tilde{\mathcal{L}}_{\mathcal{D}}(\vec{\alpha}_2)$ for all $\vec{\alpha}_1, \vec{\alpha}_2 \in \mathbb{R}^M$ and $\mu \in [0, 1]$, which is (A2). This concludes the proof. \blacksquare

Theorem A.2. Let $\mathcal{X} \equiv \mathbb{R}^d$ and $\mathcal{D} = \{(\mathbf{x}_i, y_i)\}_{i=1}^M \subseteq \mathcal{X} \times \mathbb{R}$. Given a kernel $\mathcal{K} : \mathcal{X} \times \mathcal{X} \rightarrow \mathbb{R}$, define the mean squared error $L_{\mathcal{D}} : \mathcal{R}_{\mathcal{K}} \rightarrow \mathbb{R}$ such that $L_{\mathcal{D}}(f) = \frac{1}{M} \sum_{i=1}^M (f(\mathbf{x}_i) - y_i)^2$, the regularisation term

$\Omega : \mathcal{R}_{\mathcal{K}} \rightarrow \mathbb{R}$ such that $\Omega(f) = \frac{1}{M} \|f\|_{\mathcal{R}_{\mathcal{K}}}^2$ and the regularised empirical risk functional $\mathcal{L}_{\mathcal{D}} : \mathcal{R}_{\mathcal{K}} \rightarrow \mathbb{R}$ such that $\mathcal{L}_{\mathcal{D}}(f) = L_{\mathcal{D}}(f) + \lambda\Omega(f)$ for some $\lambda > 0$. Under these conditions, the optimal model f_{opt} for \mathcal{D} in $\mathcal{R}_{\mathcal{K}}$ with respect to $\mathcal{L}_{\mathcal{D}}$ is given by

$$f_{opt}(x) = \sum_{i=1}^M \alpha_i \mathcal{K}(x, \mathbf{x}_i) \quad (\text{A4})$$

for all $x \in \mathcal{X}$ with

$$\vec{\alpha} = (K^2 + \lambda K)^+ K \vec{y}, \quad (\text{A5})$$

where $\vec{y} = (y_i)_{i=1}^M \in \mathbb{R}^M$ is the vector of training data labels, $K_{ij} = \mathcal{K}(\mathbf{x}_i, \mathbf{x}_j)$ is the kernel matrix for the input training data $\{\mathbf{x}_i\}_{i=1}^M$, and $(\cdot)^+$ is the Moore-Penrose pseudoinverse [56].

Proof. In this case the representer theorem (Theorem

4.2 in [52] and Theorem 6.11 in [53]) states that the optimal model f_{opt} for \mathcal{D} in $\mathcal{R}_{\mathcal{K}}$ with respect to $\mathcal{L}_{\mathcal{D}}$ admits a representation of the form

$$f_{\text{opt}}(\cdot) = \sum_{i=1}^M \alpha_i \mathcal{K}(\cdot, \mathbf{x}_i) \quad (\text{A6})$$

for some $\alpha_i \in \mathbb{R}$. Substituting (A6) into the regularised empirical risk functional we have that

$$\begin{aligned} \mathcal{L}_{\mathcal{D}}(f) &= \frac{1}{M} \sum_{i=1}^M \left(\sum_{j=1}^M \alpha_j \mathcal{K}(\mathbf{x}_i, \mathbf{x}_j) - y_i \right)^2 + \lambda \left\langle \sum_{k=1}^M \alpha_k \mathcal{K}(\cdot, \mathbf{x}_k), \sum_{l=1}^M \alpha_l \mathcal{K}(\cdot, \mathbf{x}_l) \right\rangle_{\mathcal{R}_{\mathcal{K}}} \\ &= \frac{1}{M} \sum_{i=1}^M \left(\sum_{j=1}^M \alpha_j \mathcal{K}(\mathbf{x}_i, \mathbf{x}_j) - y_i \right)^2 + \lambda \sum_{k,l=1}^M \alpha_k \mathcal{K}(\mathbf{x}_k, \mathbf{x}_l) \alpha_l \end{aligned}$$

At this point we can view α_i for $i \in \{1, \dots, M\}$ as variational parameters which parameterise the space of possible optimal models. This allows us to express the value of the regularised risk on this space of possible minimisers in terms of $\vec{\alpha} \in \mathbb{R}^M$ by defining $\tilde{\mathcal{L}}_{\mathcal{D}} : \mathbb{R}^M \rightarrow \mathbb{R}$ such that

$$\tilde{\mathcal{L}}_{\mathcal{D}}(\vec{\alpha}) = \frac{1}{M} \|K \vec{\alpha} - \vec{y}\|^2 + \lambda \langle \vec{\alpha}, K \vec{\alpha} \rangle, \quad (\text{A7})$$

where $\|\cdot\|$ is the Euclidean norm, $\langle \cdot, \cdot \rangle$ is the Euclidean inner product, $\vec{y} = (y_i)_{i=1}^M \in \mathbb{R}^M$ is the vector of training data labels, $K_{ij} = \mathcal{K}(\mathbf{x}_i, \mathbf{x}_j)$ is the kernel matrix for the input training data $\{\mathbf{x}_i\}_{i=1}^M$. By Theorem A.1, (A7) defines a smooth convex function $\mathbb{R}^M \rightarrow \mathbb{R}$ so we have that $\tilde{\mathcal{L}}_{\mathcal{D}}(\alpha^*)$ is the global minimum of $\tilde{\mathcal{L}}_{\mathcal{D}}$ if and only if $\nabla_{\vec{\alpha}} \tilde{\mathcal{L}}_{\mathcal{D}}(\vec{\alpha})|_{\vec{\alpha}=\alpha^*} = \vec{0}$. This implies that $\alpha^* \in \mathbb{R}^M$ satisfies

$$\begin{aligned} \frac{2}{M} K(K\alpha^* - \vec{y}) + 2\frac{\lambda}{M} K\alpha^* &= \vec{0} \\ \implies (K^2 + \lambda K)\alpha^* &= K\vec{y}. \end{aligned} \quad (\text{A8})$$

Equation (A8) may be underdetermined and not permit

a unique solution for α^* , or it may be overdetermined and not permit a solution at all. In either case, the best choice of α^* is the minimum-norm solution to

$$\arg \min_{\alpha^* \in \mathbb{R}^M} \|(K^2 + \lambda K)\alpha^* - K\vec{y}\|^2$$

which is given by

$$\alpha^* = (K^2 + \lambda K)^+ K \vec{y}$$

where $(\cdot)^+$ is the Moore-Penrose pseudo-inverse (see Chapter 5.5 of [82]). Hence the optimal model is defined by

$$f_{\text{opt}}(x) = \sum_{i=1}^M \alpha_i \mathcal{K}(x, \mathbf{x}_i)$$

for all $x \in \mathcal{X}$ with

$$\vec{\alpha} = (K^2 + \lambda K)^+ K \vec{y}$$

which is (A5). This concludes the proof. \blacksquare

Appendix B: Hyperparameter values

Kernel	Hyperparameter	Cross-validated hyperparameter values
Linear	λ	$\{0, 10^{-8}, 10^{-7}, 10^{-6}, 10^{-5}, 10^{-4}, 10^{-3}, 10^{-2}, 10^{-1}, 1, 10, 10^2, 10^3, 10^4, 10^5\}$
Polynomial	λ	$\{0, 10^{-8}, 10^{-7}, 10^{-6}, 10^{-5}, 10^{-4}, 10^{-3}, 10^{-2}, 10^{-1}, 1, 10, 10^2, 10^3, 10^4, 10^5\}$
	γ	$\{10^{-3}, 10^{-2}, 10^{-1}, 1, 10, 10^2, 10^3\}$
	c_0	$\{10^{-3}, 10^{-2}, 10^{-1}, 1, 10, 10^2, 10^3\}$
	d	$\{1, 2, 3, 4, 5, 6, 7, 8, 9, 10\}$
RBF	λ	$\{0, 10^{-8}, 10^{-7}, 10^{-6}, 10^{-5}, 10^{-4}, 10^{-3}, 10^{-2}, 10^{-1}, 1, 10, 10^2, 10^3, 10^4, 10^5\}$
	γ	$\{10^{-3}, 10^{-2}, 10^{-1}, 1, 10, 10^2, 10^3\}$
Laplacian	λ	$\{0, 10^{-8}, 10^{-7}, 10^{-6}, 10^{-5}, 10^{-4}, 10^{-3}, 10^{-2}, 10^{-1}, 1, 10, 10^2, 10^3, 10^4, 10^5\}$
	γ	$\{10^{-3}, 10^{-2}, 10^{-1}, 1, 10, 10^2, 10^3\}$
Sigmoid	λ	$\{0, 10^{-8}, 10^{-7}, 10^{-6}, 10^{-5}, 10^{-4}, 10^{-3}, 10^{-2}, 10^{-1}, 1, 10, 10^2, 10^3, 10^4, 10^5\}$
	γ	$\{10^{-3}, 10^{-2}, 10^{-1}, 1, 10, 10^2, 10^3\}$
	c_0	$\{10^{-3}, 10^{-2}, 10^{-1}, 1, 10, 10^2, 10^3\}$
Cosine	λ	$\{0, 10^{-8}, 10^{-7}, 10^{-6}, 10^{-5}, 10^{-4}, 10^{-3}, 10^{-2}, 10^{-1}, 1, 10, 10^2, 10^3, 10^4, 10^5\}$

TABLE I: Lists of hyperparameters values which were trialled during the 10-fold cross-validation performed on the training datasets. The hyperparameter λ refers to the regularisation strength which appears in (1), while the hyperparameters γ , c_0 and d correspond to those which appear in definitions of the kernels in (24), (25), (26), (27), (28) and (29).

Function	Kernel	Hyperparameter	Number of qubits (n)							
			5	10	15	20	25	30	35	40
\mathcal{O}_{XZ}	Linear	λ	10^3	10^4	10^4	10^5	10^5	10^5	10^5	10^5
		λ	10^5	1	1	1	10^{-1}	1	10^4	10^5
	Polynomial	γ	1	10^{-2}	10^{-2}	10^{-2}	10^{-2}	10^{-3}	10^{-2}	10^{-2}
		c_0	10	1	1	1	1	1	10	10
		d	6	9	6	6	6	10	6	6
		λ	10^{-2}	10^{-2}	10^{-2}	10^{-2}	10^{-2}	10^{-1}	10^{-1}	10^{-1}
		γ	1	10^{-1}	10^{-1}	10^{-2}	10^{-2}	10^{-2}	10^{-2}	10^{-2}
	RBF	λ	0	0	0	0	0	10^{-3}	10^{-3}	10^{-3}
		γ	10^{-1}	10^{-1}	10^{-1}	10^{-1}	10^{-1}	10^{-2}	10^{-2}	10^{-2}
	Laplacian	λ	0	0	0	0	0	10^{-3}	10^{-3}	10^{-3}
		γ	10^{-1}	10^{-1}	10^{-1}	10^{-1}	10^{-1}	10^{-2}	10^{-2}	10^{-2}
	Sigmoid	λ	10^{-4}	10^{-6}	10^{-5}	0	10^{-5}	10^{-8}	10^{-1}	1
		γ	10^{-2}	10^{-2}	10^{-3}	10^{-3}	10^{-3}	10^{-3}	10^{-3}	10^{-3}
		c_0	10^{-1}	1	1	10^{-1}	1	1	10^{-1}	1
	Cosine	λ	10^2	10^3	10^3	10^3	10^3	10^3	10^2	10^2
\mathcal{O}_{Sum}	Linear	λ	10^3	10^4	10^4	10^4	10^5	10^5	10^5	10^5
		λ	1	10^{-3}	1	10^{-2}	10^{-1}	1	1	1
	Polynomial	γ	10^{-1}	10^{-2}	10^{-2}	10^{-3}	10^{-3}	10^{-3}	10^{-3}	10^{-3}
		c_0	1	1	1	1	1	1	1	1
		d	8	8	8	10	10	10	9	8
		λ	10^{-3}	10^{-1}	10^{-2}	10^{-2}	10^{-2}	10^{-1}	10^{-1}	10^{-1}
		γ	10^{-1}	10^{-1}	10^{-1}	10^{-2}	10^{-2}	10^{-2}	10^{-2}	10^{-2}
	RBF	λ	10^{-8}	0	0	0	0	10^{-3}	10^{-3}	10^{-3}
		γ	10^{-1}	10^{-1}	10^{-1}	10^{-1}	10^{-1}	10^{-2}	10^{-2}	10^{-2}
	Laplacian	λ	0	0	0	0	0	10^{-3}	10^{-3}	10^{-3}
		γ	10^{-1}	10^{-1}	10^{-1}	10^{-1}	10^{-1}	10^{-2}	10^{-2}	10^{-2}
	Sigmoid	λ	1	10^{-6}	10^{-5}	0	10^{-5}	10^{-6}	10^{-1}	1
		γ	10^{-1}	10^{-2}	10^{-3}	10^{-3}	10^{-3}	10^{-3}	10^{-3}	10^{-3}
		c_0	10^{-1}	1	1	10^{-1}	1	1	10^{-1}	1
	Cosine	λ	10^2	10^3	10^3	10^3	10^3	10^3	10^2	10^2

TABLE II: The best hyperparameters trialled during the 10-fold cross-validation performed on the training datasets for \mathcal{H}_1 . Of all the hyperparameters trialled, the ones listed here resulted in models which achieved the highest average coefficient of determination (R^2) over all 10 folds of the training dataset.

Function	Kernel	Hyperparameter	Number of qubits (n)							
			5	10	15	20	25	30	35	40
\mathcal{O}_{XZ}	Linear	λ	10^4	10^4	10^5	10^5	10^5	10^5	10^5	10^5
	Polynomial	λ	10^5	10^{-1}	1	10^{-2}	10^{-1}	10^{-1}	10^5	10^5
		γ	1	10^{-2}	10^{-2}	10^{-3}	10^{-3}	10^{-3}	10^{-2}	10^{-2}
		c_0	10	1	1	1	1	1	10	10
		d	6	7	6	10	9	7	6	6
	RBF	λ	10^{-3}	10^{-1}	10^{-2}	10^{-2}	10^{-1}	10^{-1}	10^{-1}	10^{-1}
		γ	1	10^{-1}	10^{-1}	10^{-2}	10^{-2}	10^{-2}	10^{-2}	10^{-2}
	Laplacian	λ	0	10^{-1}	10^{-2}	10^{-2}	0	0	0	10^{-2}
		γ	1	10^{-1}	10^{-1}	10^{-1}	10^{-1}	10^{-1}	10^{-1}	10^{-2}
	Sigmoid	λ	1	10^{-8}	10^{-4}	10^{-8}	10^{-5}	10^{-6}	10^{-2}	1
		γ	10^{-1}	10^{-2}	10^{-3}	10^{-3}	10^{-3}	10^{-3}	10^{-3}	10^{-3}
		c_0	10^{-1}	1	10^{-1}	10^{-1}	1	1	1	1
	Cosine	λ	10^3	10^3	10^3	10^4	10^4	10^4	10^4	10^5
\mathcal{O}_{Sum}	Linear	λ	10^4	10^4	10^5	10^5	10^5	10^5	10^5	10^5
	Polynomial	λ	1	10^5	10^4	10^{-4}	10^{-2}	10^{-2}	10^4	10^3
		γ	10^{-1}	10^{-1}	10^{-2}	10^{-3}	10^{-3}	10^{-3}	10^{-3}	10^{-3}
		c_0	1	10	10	1	1	1	10	10
		d	8	8	8	6	7	6	9	8
	RBF	λ	10^{-3}	10^{-1}	10^{-2}	10^{-2}	10^{-1}	10^{-1}	10^{-1}	10^{-1}
		γ	1	10^{-1}	10^{-1}	10^{-2}	10^{-2}	10^{-2}	10^{-2}	10^{-2}
	Laplacian	λ	10^{-1}	10^{-1}	10^{-2}	10^{-2}	0	10^{-2}	10^{-2}	10^{-2}
		γ	10^{-1}	10^{-1}	10^{-1}	10^{-1}	10^{-1}	10^{-2}	10^{-2}	10^{-2}
	Sigmoid	λ	0	10^{-7}	10^{-5}	10^{-8}	10^{-5}	10^{-6}	10^{-2}	1
		γ	10^{-2}	10^{-2}	10^{-3}	10^{-3}	10^{-3}	10^{-3}	10^{-3}	10^{-3}
		c_0	10^{-1}	1	1	10^{-1}	1	1	1	1
	Cosine	λ	10^3	10^3	10^4	10^4	10^4	10^5	10^4	10^5

TABLE III: The best hyperparameters trialled during the 10-fold cross-validation performed on the training datasets for \mathcal{H}_2 . Of all the hyperparameters trialled, the ones listed here resulted in models which achieved the highest average coefficient of determination (R^2) over all 10 folds of the training dataset.

Function	Kernel	Hyperparameter	Number of qubits (n)							
			5	10	15	20	25	30	35	40
\mathcal{O}_{XZ}	Linear	λ	10^4	10^5	10^5	10^5	10^5	10^5	10^5	10^5
		λ	10^5	10^{-1}	1	1	10^{-1}	1	1	1
	Polynomial	γ	1	10^{-2}	10^{-2}	10^{-2}	10^{-3}	10^{-3}	10^{-3}	10^{-3}
		c_0	10	1	1	1	1	1	1	1
		d	6	7	6	6	10	10	9	8
		RBF	λ	10^{-2}	10^{-2}	10^{-2}	10^{-3}	10^{-2}	10^{-2}	10^{-2}
			γ	1	10^{-1}	10^{-1}	10^{-2}	10^{-2}	10^{-2}	10^{-2}
	Laplacian	λ	0	0	0	0	0	0	0	0
		γ	1	10^{-1}	10^{-1}	10^{-1}	10^{-1}	10^{-1}	10^{-1}	10^{-1}
	Sigmoid	λ	1	10^{-6}	10^{-5}	10^{-8}	10^{-5}	0	10^{-6}	1
		γ	10^{-1}	10^{-2}	10^{-3}	10^{-3}	10^{-3}	10^{-3}	10^{-3}	10^{-3}
		c_0	10^{-1}	1	1	10^{-1}	1	1	1	1
	Cosine	λ	10^3	10^3	10^4	10^4	10^4	10^4	10^4	10^4
\mathcal{O}_{Sum}	Linear	λ	10^4	10^5	10^5	10^5	10^5	10^5	10^5	10^5
		λ	1	10^5	1	10	10^5	10^5	10^{-2}	10^{-2}
	Polynomial	γ	10^{-1}	10^{-1}	10^{-2}	10^{-2}	10^{-2}	10^{-2}	10^{-3}	10^{-3}
		c_0	1	10	1	1	10	10	1	1
		d	8	8	8	8	9	8	8	8
		RBF	λ	10^{-3}	10^{-2}	10^{-2}	10^{-3}	10^{-2}	10^{-2}	10^{-2}
			γ	1	10^{-1}	10^{-1}	10^{-2}	10^{-2}	10^{-2}	10^{-2}
	Laplacian	λ	0	0	0	0	0	0	0	0
		γ	1	10^{-1}	10^{-1}	10^{-1}	10^{-1}	10^{-1}	10^{-1}	10^{-1}
	Sigmoid	λ	1	10^{-6}	10^{-5}	10^{-8}	10^{-5}	0	10^{-6}	1
		γ	10^{-1}	10^{-2}	10^{-3}	10^{-3}	10^{-3}	10^{-3}	10^{-3}	10^{-3}
		c_0	10^{-1}	1	1	10^{-1}	1	1	1	1
	Cosine	λ	10^4	10^5	10^5	10^5	10^4	10^4	10^4	10^4

TABLE IV: The best hyperparameters trialled during the 10-fold cross-validation performed on the training datasets for \mathcal{H}_3 . Of all the hyperparameters trialled, the ones listed here resulted in models which achieved the highest average coefficient of determination (R^2) over all 10 folds of the training dataset.

Function	Kernel	Hyperparameter	Number of qubits (n)							
			5	10	15	20	25	30	35	40
\mathcal{O}_{XZ}	Linear	λ	10^4	10^4	10^5	10^5	10^5	10^5	10^5	10^5
		λ	10^{-2}	10^{-2}	1	10	10^5	10	10^5	10^5
	Polynomial	γ	10^{-2}	10^{-3}	10^{-3}	10^{-3}	10^{-2}	10^{-3}	10^{-3}	10^{-3}
		c_0	1	1	1	1	10	1	10	10
	RBF	d	6	10	9	9	6	6	9	8
		λ	10^{-1}	10^{-2}	10^{-2}	10^{-2}	10^{-2}	10^{-2}	10^{-2}	10^{-2}
	Laplacian	γ	10^{-1}	10^{-2}	10^{-2}	10^{-2}	10^{-3}	10^{-3}	10^{-3}	10^{-3}
\mathcal{O}_{Sum}	Sigmoid	λ	0	0	10^{-3}	10^{-3}	10^{-3}	10^{-3}	10^{-3}	10^{-4}
		γ	10^{-1}	10^{-1}	10^{-2}	10^{-2}	10^{-2}	10^{-2}	10^{-2}	10^{-2}
	Cosine	λ	10^{-6}	10^{-8}	10^{-5}	1	1	10	10^{-7}	10
		γ	10^{-2}	10^{-3}	10^{-3}	10^{-3}	10^{-3}	10^{-3}	10^{-3}	10^{-3}
	Linear	c_0	1	10^{-1}	1	1	10^{-1}	1	10	1
		λ	10^3	10^3	10^3	10^3	10^3	10^3	10^3	10^3
	Polynomial	λ	10^{-2}	10^{-2}	1	10	10	10^5	10^4	10^5
		γ	10^{-2}	10^{-3}	10^{-3}	10^{-3}	10^{-3}	10^{-3}	10^{-3}	10^{-3}
	RBF	c_0	1	1	1	1	10	10	10	10
		d	9	9	9	8	6	8	7	7
	Laplacian	λ	10^{-1}	10^{-2}	10^{-2}	10^{-2}	10^{-2}	10^{-2}	10^{-2}	10^{-2}
		γ	10^{-1}	10^{-2}	10^{-2}	10^{-2}	10^{-3}	10^{-3}	10^{-3}	10^{-3}
	Sigmoid	λ	0	0	10^{-3}	10^{-3}	10^{-3}	10^{-3}	10^{-8}	10^{-8}
		γ	10^{-1}	10^{-1}	10^{-2}	10^{-2}	10^{-2}	10^{-2}	10^{-2}	10^{-2}
	Cosine	λ	10^{-6}	10^{-8}	10^{-5}	1	1	10	10^{-7}	10
		γ	10^{-2}	10^{-3}	10^{-3}	10^{-3}	10^{-3}	10^{-3}	10^{-3}	10^{-3}
		c_0	1	10^{-1}	1	1	10^{-1}	1	10	1

TABLE V: The best hyperparameters trialled during the 10-fold cross-validation performed on the training datasets for \mathcal{H}_4 . Of all the hyperparameters trialled, the ones listed here resulted in models which achieved the highest average coefficient of determination (R^2) over all 10 folds of the training dataset.

Appendix C: Numerical results

1. Results for \mathcal{O}_{XZ} and \mathcal{H}_1

Dataset	Kernel	Metric	Number of qubits (n)							
			5	10	15	20	25	30	35	40
Testing	Linear	RMSE	0.7886	0.8122	0.8156	0.8214	0.8156	0.8147	0.8030	0.7941
		MAE	0.7091	0.7296	0.7275	0.7307	0.7186	0.7159	0.6991	0.6857
		R^2	-1.9284	-4.1339	-3.5942	-3.7616	-3.4297	-3.3197	-3.0432	-2.8091
	Polynomial	RMSE	0.1722	0.1493	0.1755	0.1563	0.1669	0.1694	0.1716	0.1775
		MAE	0.1228	0.1076	0.1185	0.1121	0.1200	0.1191	0.1249	0.1274
		R^2	0.8604	0.8265	0.7872	0.8276	0.8145	0.8132	0.8154	0.8097
	RBF	RMSE	0.0867	0.0837	0.1256	0.1212	0.1359	0.1216	0.1191	0.1117
		MAE	0.0431	0.0489	0.0586	0.0772	0.0790	0.0739	0.0674	0.0594
		R^2	0.9646	0.9454	0.8910	0.8963	0.8771	0.9038	0.9111	0.9246
	Laplacian	RMSE	0.1137	0.0625	0.1057	0.0801	0.0983	0.0990	0.0978	0.0871
		MAE	0.0763	0.0388	0.0495	0.0463	0.0529	0.0660	0.0636	0.0559
		R^2	0.9391	0.9696	0.9228	0.9547	0.9356	0.9362	0.9401	0.9542
	Sigmoid	RMSE	0.2616	0.1322	0.2259	0.1601	0.1669	0.1538	0.2240	0.2441
		MAE	0.1852	0.0895	0.1617	0.1123	0.1176	0.1081	0.1696	0.1899
		R^2	0.6777	0.8639	0.6475	0.8191	0.8144	0.8461	0.6852	0.6400
	Cosine	RMSE	0.7916	0.8117	0.8135	0.8218	0.8153	0.8139	0.8066	0.7971
		MAE	0.7116	0.7285	0.7240	0.7306	0.7175	0.7136	0.7024	0.6882
		R^2	-1.9508	-4.1287	-3.5710	-3.7659	-3.4271	-3.3113	-3.0796	-2.8382
Training	Linear	RMSE	0.7692	0.7919	0.7971	0.8052	0.8025	0.7979	0.7870	0.7745
		MAE	0.6823	0.6985	0.6996	0.7035	0.6971	0.6893	0.6750	0.6589
		R^2	-1.7147	-3.4479	-3.1980	-3.1767	-2.9977	-2.8207	-2.6211	-2.4198
	Polynomial	RMSE	0.1519	0.1329	0.1398	0.1414	0.1439	0.1426	0.1520	0.1583
		MAE	0.1071	0.0939	0.0992	0.1006	0.1035	0.0997	0.1078	0.1110
		R^2	0.8942	0.8747	0.8709	0.8712	0.8715	0.8779	0.8650	0.8572
	RBF	RMSE	0.0077	0.0334	0.0138	0.0809	0.0667	0.0723	0.0580	0.0476
		MAE	0.0049	0.0224	0.0078	0.0557	0.0452	0.0491	0.0390	0.0308
		R^2	0.9997	0.9921	0.9987	0.9578	0.9724	0.9686	0.9803	0.9871
	Laplacian	RMSE	0.0000	0.0000	0.0000	0.0000	0.0000	0.0075	0.0059	0.0047
		MAE	0.0000	0.0000	0.0000	0.0000	0.0000	0.0054	0.0042	0.0033
		R^2	1.0000	1.0000	1.0000	1.0000	1.0000	0.9997	0.9998	0.9999
	Sigmoid	RMSE	0.2539	0.0912	0.2056	0.1380	0.1423	0.1204	0.2177	0.2544
		MAE	0.1791	0.0666	0.1470	0.0996	0.1009	0.0881	0.1567	0.1892
		R^2	0.7042	0.9410	0.7206	0.8773	0.8743	0.9130	0.7229	0.6310
	Cosine	RMSE	0.7690	0.7923	0.7979	0.8052	0.8027	0.7983	0.7860	0.7736
		MAE	0.6816	0.6983	0.6983	0.7030	0.6961	0.6873	0.6746	0.6578
		R^2	-1.7129	-3.4530	-3.2072	-3.1761	-2.9999	-2.8250	-2.6125	-2.4122

TABLE VI: Learning performance metrics for the models trained with the hyperparameters listed in Table II for \mathcal{O}_{XZ} . The metrics are calculated based on the predictions made by the models on the training and testing sets for \mathcal{H}_1 with labels determined by \mathcal{O}_{XZ} . The best values for each qubit number and each metric are in bold text for the training and testing datasets. All values in this table are plotted in Figure 6, though not all of them are visible within the chosen plot range.

2. Results for \mathcal{O}_{Sum} and \mathcal{H}_1

Dataset	Kernel	Metric	Number of qubits (n)							
			5	10	15	20	25	30	35	40
Testing	Linear	RMSE	6.6797	7.2117	7.2580	7.3482	7.2775	7.2564	7.1498	7.0573
		MAE	5.8351	6.4148	6.4226	6.5026	6.3839	6.3326	6.1876	6.0515
		R^2	-2.6121	-3.7405	-3.5677	-3.5157	-3.3017	-3.1259	-2.8970	-2.6603
	Polynomial	RMSE	0.9266	1.1954	1.2084	1.4719	1.4644	1.5292	1.5170	1.5602
		MAE	0.6546	0.8219	0.8558	1.0416	1.0461	1.0767	1.0694	1.1116
		R^2	0.9305	0.8697	0.8734	0.8188	0.8258	0.8168	0.8246	0.8211
	RBF	RMSE	0.7402	0.8833	0.8885	1.1049	1.1179	1.0755	1.0196	0.9878
		MAE	0.5409	0.4966	0.4385	0.6916	0.6624	0.6367	0.5657	0.5190
		R^2	0.9556	0.9289	0.9315	0.8979	0.8985	0.9094	0.9208	0.9283
	Laplacian	RMSE	0.6841	0.6176	0.6979	0.7291	0.7592	0.8534	0.8078	0.7417
		MAE	0.4643	0.3579	0.3771	0.3990	0.4168	0.5653	0.5250	0.4746
		R^2	0.9621	0.9652	0.9578	0.9555	0.9532	0.9429	0.9503	0.9596
Training	Sigmoid	RMSE	1.7673	1.1875	1.9128	1.4774	1.4508	1.3716	2.0234	2.2092
		MAE	1.3062	0.7939	1.4378	1.0354	1.0400	0.9645	1.5305	1.7456
		R^2	0.7472	0.8715	0.6827	0.8175	0.8290	0.8526	0.6879	0.6413
	Cosine	RMSE	6.7042	7.2079	7.2421	7.3244	7.2756	7.2927	7.1820	7.0846
		MAE	5.8541	6.4031	6.3958	6.4589	6.3751	6.3714	6.2191	6.0739
		R^2	-2.6387	-3.7354	-3.5476	-3.4864	-3.2995	-3.1673	-2.9321	-2.6887
	Linear	RMSE	6.4890	7.0385	7.0937	7.1710	7.1516	7.1017	6.9922	6.8715
		MAE	5.5720	6.1532	6.1925	6.2540	6.1792	6.1015	5.9658	5.8112
		R^2	-2.1828	-3.1641	-3.0659	-2.9840	-2.8636	-2.6929	-2.5129	-2.3154
	Polynomial	RMSE	0.7307	0.8701	0.9015	1.2510	1.2271	1.2795	1.2360	1.2827
		MAE	0.5112	0.6282	0.6547	0.8919	0.8785	0.8960	0.8745	0.9044
		R^2	0.9596	0.9364	0.9343	0.8788	0.8862	0.8801	0.8902	0.8845
	RBF	RMSE	0.5713	0.4603	0.1088	0.7159	0.5706	0.6236	0.4932	0.4137
		MAE	0.4250	0.3093	0.0643	0.4913	0.3904	0.4216	0.3307	0.2663
		R^2	0.9753	0.9822	0.9990	0.9603	0.9754	0.9715	0.9825	0.9880
	Laplacian	RMSE	0.0000	0.0000	0.0000	0.0000	0.0000	0.0648	0.0492	0.0397
		MAE	0.0000	0.0000	0.0000	0.0000	0.0000	0.0463	0.0352	0.0279
		R^2	1.0000	1.0000	1.0000	1.0000	1.0000	0.9997	0.9998	0.9999
	Sigmoid	RMSE	1.8283	0.8245	1.8096	1.2541	1.2770	1.0701	1.9611	2.2970
		MAE	1.3103	0.5973	1.3112	0.9025	0.9082	0.7856	1.4166	1.7306
		R^2	0.7473	0.9429	0.7354	0.8782	0.8768	0.9162	0.7237	0.6295
	Cosine	RMSE	6.4854	7.0431	7.1016	7.1794	7.1538	7.0918	6.9837	6.8637
		MAE	5.5633	6.1464	6.1758	6.2249	6.1695	6.1030	5.9616	5.8011
		R^2	-2.1793	-3.1696	-3.0751	-2.9934	-2.8659	-2.6827	-2.5044	-2.3079

TABLE VII: Learning performance metrics for the models trained with the hyperparameters listed in Table II for \mathcal{O}_{Sum} . The metrics are calculated based on the predictions made by the models on the training and testing sets for \mathcal{H}_1 with labels determined by \mathcal{O}_{Sum} . The best values for each qubit number and each metric are in bold text for the training and testing datasets. All values in this table are plotted in Figure 7, though not all of them are visible within the chosen plot range.

3. Results for \mathcal{O}_{XZ} and \mathcal{H}_2

Dataset	Kernel	Metric	Number of qubits (n)							
			5	10	15	20	25	30	35	40
Testing	Linear	RMSE	0.7436	0.7882	0.8055	0.8159	0.8166	0.8162	0.8148	0.8127
		MAE	0.6594	0.7145	0.7385	0.7505	0.7493	0.7454	0.7407	0.7354
		R^2	-2.1150	-3.8313	-4.6197	-4.9758	-4.8876	-4.6711	-4.4779	-4.2726
	Polynomial	RMSE	0.2462	0.2088	0.1877	0.1703	0.1717	0.1731	0.1741	0.1683
		MAE	0.1804	0.1481	0.1335	0.1248	0.1230	0.1264	0.1278	0.1254
		R^2	0.6585	0.6609	0.6947	0.7395	0.7397	0.7450	0.7500	0.7739
	RBF	RMSE	0.0782	0.1308	0.1399	0.1232	0.1202	0.1152	0.1123	0.1065
		MAE	0.0457	0.0848	0.0894	0.0865	0.0827	0.0804	0.0740	0.0695
		R^2	0.9656	0.8670	0.8306	0.8638	0.8725	0.8869	0.8959	0.9095
	Laplacian	RMSE	0.1355	0.1372	0.1337	0.1179	0.1149	0.1100	0.1110	0.1232
		MAE	0.0839	0.0920	0.0858	0.0778	0.0744	0.0709	0.0716	0.0880
		R^2	0.8965	0.8536	0.8452	0.8751	0.8834	0.8970	0.8982	0.8789
	Sigmoid	RMSE	0.3297	0.1771	0.2385	0.1724	0.1671	0.1482	0.2161	0.2327
		MAE	0.2513	0.1221	0.1712	0.1254	0.1198	0.1063	0.1541	0.1646
		R^2	0.3878	0.7562	0.5072	0.7333	0.7533	0.8132	0.6145	0.5679
	Cosine	RMSE	0.7445	0.7888	0.8067	0.8158	0.8165	0.8161	0.8144	0.8122
		MAE	0.6603	0.7146	0.7396	0.7502	0.7488	0.7447	0.7400	0.7343
		R^2	-2.1225	-3.8386	-4.6360	-4.9752	-4.8860	-4.6687	-4.4737	-4.2664
Training	Linear	RMSE	0.7533	0.7960	0.8159	0.8177	0.8237	0.8204	0.8194	0.8164
		MAE	0.6691	0.7256	0.7532	0.7537	0.7588	0.7515	0.7479	0.7414
		R^2	-2.0465	-3.9309	-5.1218	-5.1428	-5.2954	-4.9662	-4.8482	-4.5928
	Polynomial	RMSE	0.2321	0.2011	0.1691	0.1580	0.1565	0.1598	0.1589	0.1560
		MAE	0.1741	0.1374	0.1204	0.1111	0.1100	0.1115	0.1125	0.1123
		R^2	0.7107	0.6852	0.7371	0.7708	0.7728	0.7736	0.7800	0.7957
	RBF	RMSE	0.0035	0.1112	0.0215	0.1018	0.0968	0.0862	0.0702	0.0578
		MAE	0.0020	0.0663	0.0124	0.0649	0.0642	0.0556	0.0457	0.0368
		R^2	0.9999	0.9037	0.9958	0.9047	0.9131	0.9341	0.9571	0.9720
	Laplacian	RMSE	0.0000	0.0765	0.0087	0.0060	0.0000	0.0000	0.0000	0.0355
		MAE	0.0000	0.0485	0.0058	0.0038	0.0000	0.0000	0.0000	0.0259
		R^2	1.0000	0.9544	0.9993	0.9997	1.0000	1.0000	1.0000	0.9894
	Sigmoid	RMSE	0.3343	0.1586	0.2264	0.1580	0.1554	0.1277	0.1979	0.2320
		MAE	0.2581	0.1065	0.1629	0.1132	0.1097	0.0874	0.1414	0.1670
		R^2	0.4002	0.8042	0.5287	0.7707	0.7758	0.8554	0.6587	0.5484
	Cosine	RMSE	0.7530	0.7963	0.8156	0.8183	0.8244	0.8212	0.8202	0.8174
		MAE	0.6687	0.7265	0.7530	0.7546	0.7600	0.7529	0.7493	0.7428
		R^2	-2.0444	-3.9348	-5.1180	-5.1514	-5.3066	-4.9779	-4.8603	-4.6056

TABLE VIII: Learning performance metrics for the models trained with the hyperparameters listed in Table III for \mathcal{O}_{XZ} . The metrics are calculated based on the predictions made by the models on the training and testing sets for \mathcal{H}_2 with labels determined by \mathcal{O}_{XZ} . The best values for each qubit number and each metric are in bold text for the training and testing datasets. All values in this table are plotted in Figure 8, though not all of them are visible within the chosen plot range.

4. Results for \mathcal{O}_{Sum} and \mathcal{H}_2

Dataset	Kernel	Metric	Number of qubits (n)							
			5	10	15	20	25	30	35	40
Testing	Linear	RMSE	6.6084	6.9384	7.1717	7.2117	7.2634	7.2450	7.2467	7.2143
		MAE	5.7357	6.2669	6.5641	6.6096	6.6403	6.5921	6.5668	6.5059
		R^2	-2.4632	-4.3090	-5.1549	-5.2246	-5.0555	-4.7658	-4.5452	-4.3089
	Polynomial	RMSE	1.4942	1.1867	1.3563	1.2833	1.3342	1.3341	1.7604	1.4036
		MAE	1.1004	0.8443	1.0029	0.9740	1.0096	1.0189	1.2957	1.0740
		R^2	0.8230	0.8447	0.7799	0.8029	0.7957	0.8045	0.6727	0.7990
	RBF	RMSE	0.6089	0.9284	0.9039	0.9337	0.9487	0.9708	0.9471	0.9099
		MAE	0.3170	0.6004	0.5720	0.6676	0.6700	0.6674	0.6390	0.6063
		R^2	0.9706	0.9049	0.9022	0.8957	0.8967	0.8965	0.9053	0.9156
	Laplacian	RMSE	1.0664	0.9648	0.9189	0.8730	0.8813	1.0177	1.0370	1.0398
		MAE	0.7712	0.6657	0.6309	0.6007	0.5915	0.7304	0.7410	0.7411
		R^2	0.9098	0.8973	0.8990	0.9088	0.9108	0.8862	0.8865	0.8897
	Sigmoid	RMSE	2.5193	1.1984	1.9133	1.2459	1.2601	1.2474	1.8645	2.0244
		MAE	1.9383	0.8575	1.3799	0.9470	0.9429	0.8848	1.3602	1.4461
		R^2	0.4967	0.8416	0.5619	0.8142	0.8178	0.8291	0.6329	0.5820
	Cosine	RMSE	6.6158	6.9427	7.1717	7.2107	7.2616	7.2411	7.2422	7.2080
		MAE	5.7417	6.2682	6.5637	6.6062	6.6348	6.5832	6.5569	6.4933
		R^2	-2.4709	-4.3156	-5.1549	-5.2228	-5.0525	-4.7597	-4.5384	-4.2995
Training	Linear	RMSE	6.6747	6.9451	7.2232	7.2249	7.2857	7.2512	7.2503	7.2167
		MAE	5.7924	6.2699	6.6278	6.6248	6.6670	6.6053	6.5781	6.5165
		R^2	-2.5404	-4.3985	-5.3317	-5.2921	-5.1667	-4.8959	-4.6703	-4.4283
	Polynomial	RMSE	1.2201	1.0716	1.3412	1.2795	1.3206	1.3084	1.6460	1.3672
		MAE	0.9328	0.7624	0.9493	0.9258	0.9539	0.9551	1.2068	1.0022
		R^2	0.8817	0.8715	0.7817	0.8027	0.7974	0.8080	0.7078	0.8052
	RBF	RMSE	0.0252	0.7066	0.1727	0.7663	0.7902	0.6823	0.5885	0.4879
		MAE	0.0142	0.4788	0.1020	0.5265	0.5465	0.4763	0.4020	0.3227
		R^2	0.9999	0.9441	0.9964	0.9292	0.9275	0.9478	0.9626	0.9752
	Laplacian	RMSE	0.7618	0.4858	0.0639	0.0435	0.0000	0.3533	0.3186	0.2906
		MAE	0.5515	0.3406	0.0450	0.0301	0.0000	0.2641	0.2397	0.2191
		R^2	0.9539	0.9736	0.9995	0.9998	1.0000	0.9860	0.9891	0.9912
	Sigmoid	RMSE	2.4146	1.0306	1.8288	1.2287	1.2850	1.0282	1.7178	2.0124
		MAE	1.8768	0.7487	1.3039	0.8932	0.9275	0.7365	1.2508	1.4609
		R^2	0.5367	0.8811	0.5941	0.8180	0.8082	0.8815	0.6817	0.5779
	Cosine	RMSE	6.6723	6.9480	7.2267	7.2301	7.2915	7.2585	7.2572	7.2243
		MAE	5.7902	6.2753	6.6324	6.6318	6.6754	6.6159	6.5880	6.5268
		R^2	-2.5378	-4.4031	-5.3380	-5.3013	-5.1766	-4.9077	-4.6811	-4.4397

TABLE IX: Learning performance metrics for the models trained with the hyperparameters listed in Table III for \mathcal{O}_{Sum} . The metrics are calculated based on the predictions made by the models on the training and testing sets for \mathcal{H}_2 with labels determined by \mathcal{O}_{Sum} . The best values for each qubit number and each metric are in bold text for the training and testing datasets. All values in this table are plotted in Figure 9, though not all of them are visible within the chosen plot range.

5. Results for \mathcal{O}_{XZ} and \mathcal{H}_3

Dataset	Kernel	Metric	Number of qubits (n)							
			5	10	15	20	25	30	35	40
Testing	Linear	RMSE	0.6230	0.6630	0.6810	0.6884	0.6873	0.6775	0.6611	0.6408
		MAE	0.5066	0.5423	0.5542	0.5567	0.5506	0.5349	0.5117	0.4843
		R^2	-1.5252	-1.9782	-1.9471	-1.8755	-1.7657	-1.6170	-1.4506	-1.2877
	Polynomial	RMSE	0.1792	0.1395	0.1376	0.1402	0.1392	0.1436	0.1429	0.1480
		MAE	0.1323	0.1031	0.1035	0.1066	0.1054	0.1076	0.1059	0.1080
		R^2	0.7911	0.8681	0.8797	0.8807	0.8866	0.8824	0.8855	0.8780
	RBF	RMSE	0.0608	0.0502	0.0459	0.0724	0.0655	0.0633	0.0598	0.0564
		MAE	0.0379	0.0354	0.0290	0.0511	0.0452	0.0430	0.0384	0.0347
		R^2	0.9760	0.9829	0.9866	0.9682	0.9749	0.9772	0.9799	0.9823
	Laplacian	RMSE	0.0843	0.0780	0.0704	0.0679	0.0671	0.0670	0.0675	0.0688
		MAE	0.0573	0.0570	0.0498	0.0470	0.0456	0.0445	0.0431	0.0424
		R^2	0.9537	0.9588	0.9685	0.9720	0.9736	0.9744	0.9745	0.9736
	Sigmoid	RMSE	0.1965	0.1105	0.1727	0.1417	0.1415	0.1257	0.1085	0.2197
		MAE	0.1504	0.0835	0.1336	0.1067	0.1092	0.0975	0.0818	0.1781
		R^2	0.7489	0.9173	0.8105	0.8782	0.8828	0.9099	0.9340	0.7311
	Cosine	RMSE	0.6234	0.6635	0.6810	0.6884	0.6873	0.6775	0.6611	0.6407
		MAE	0.5068	0.5431	0.5539	0.5561	0.5493	0.5326	0.5087	0.4808
		R^2	-1.5284	-1.9820	-1.9474	-1.8757	-1.7659	-1.6170	-1.4505	-1.2875
Training	Linear	RMSE	0.6146	0.6641	0.6847	0.6934	0.6927	0.6825	0.6646	0.6424
		MAE	0.5005	0.5452	0.5581	0.5607	0.5547	0.5390	0.5154	0.4871
		R^2	-1.5555	-2.0435	-1.9755	-1.8833	-1.7698	-1.6269	-1.4667	-1.3070
	Polynomial	RMSE	0.1640	0.1285	0.1270	0.1279	0.1251	0.1293	0.1270	0.1301
		MAE	0.1217	0.0954	0.0960	0.0984	0.0952	0.0969	0.0949	0.0966
		R^2	0.8181	0.8861	0.8976	0.9018	0.9097	0.9057	0.9100	0.9054
	RBF	RMSE	0.0108	0.0282	0.0118	0.0506	0.0474	0.0377	0.0282	0.0196
		MAE	0.0070	0.0190	0.0069	0.0355	0.0322	0.0255	0.0185	0.0123
		R^2	0.9992	0.9945	0.9991	0.9847	0.9871	0.9920	0.9956	0.9979
	Laplacian	RMSE	0.0000	0.0000	0.0000	0.0000	0.0000	0.0000	0.0000	0.0000
		MAE	0.0000	0.0000	0.0000	0.0000	0.0000	0.0000	0.0000	0.0000
		R^2	1.0000	1.0000	1.0000	1.0000	1.0000	1.0000	1.0000	1.0000
	Sigmoid	RMSE	0.2169	0.0894	0.1814	0.1245	0.1321	0.1071	0.0888	0.2324
		MAE	0.1649	0.0693	0.1367	0.0965	0.1015	0.0839	0.0691	0.1849
		R^2	0.6817	0.9448	0.7911	0.9070	0.8992	0.9353	0.9559	0.6980
	Cosine	RMSE	0.6143	0.6637	0.6849	0.6936	0.6929	0.6828	0.6649	0.6427
		MAE	0.5001	0.5450	0.5582	0.5607	0.5541	0.5375	0.5130	0.4840
		R^2	-1.5528	-2.0398	-1.9766	-1.8849	-1.7718	-1.6290	-1.4689	-1.3090

TABLE X: Learning performance metrics for the models trained with the hyperparameters listed in Table IV for \mathcal{O}_{XZ} . The metrics are calculated based on the predictions made by the models on the training and testing sets for \mathcal{H}_3 with labels determined by \mathcal{O}_{XZ} . The best values for each qubit number and each metric are in bold text for the training and testing datasets. All values in this table are plotted in Figure 10, though not all of them are visible within the chosen plot range.

6. Results for \mathcal{O}_{Sum} and \mathcal{H}_3

Dataset	Kernel	Metric	Number of qubits (n)							
			5	10	15	20	25	30	35	40
Testing	Linear	RMSE	5.2940	5.8909	6.0765	6.1494	6.1253	6.0140	5.8459	5.6489
		MAE	4.2697	4.8224	4.9492	4.9773	4.9052	4.7378	4.5049	4.2420
		R^2	-1.8253	-2.0274	-1.9619	-1.8855	-1.7631	-1.5998	-1.4225	-1.2536
	Polynomial	RMSE	1.1585	0.9611	0.9857	0.9956	0.9778	1.0404	1.0888	1.1037
		MAE	0.8594	0.7375	0.7432	0.7518	0.7466	0.7980	0.8239	0.8420
		R^2	0.8647	0.9194	0.9221	0.9244	0.9296	0.9222	0.9160	0.9140
	RBF	RMSE	0.3834	0.3908	0.3831	0.6243	0.5514	0.5142	0.4808	0.4614
		MAE	0.2247	0.2704	0.2342	0.4376	0.3829	0.3485	0.3089	0.2831
		R^2	0.9852	0.9867	0.9882	0.9703	0.9776	0.9810	0.9836	0.9850
	Laplacian	RMSE	0.6000	0.6719	0.6060	0.5842	0.5770	0.5740	0.5768	0.5884
		MAE	0.3753	0.4879	0.4285	0.4042	0.3895	0.3767	0.3644	0.3564
		R^2	0.9637	0.9606	0.9705	0.9740	0.9755	0.9763	0.9764	0.9755
	Sigmoid	RMSE	1.5850	0.9691	1.5702	1.2545	1.2594	1.1208	0.9594	1.9734
		MAE	1.1870	0.7475	1.2129	0.9506	0.9707	0.8719	0.7301	1.6113
		R^2	0.7468	0.9181	0.8022	0.8799	0.8832	0.9097	0.9348	0.7250
	Cosine	RMSE	5.2944	5.8910	6.0766	6.1494	6.1255	6.0142	5.8459	5.6488
		MAE	4.2685	4.8210	4.9456	4.9710	4.8940	4.7187	4.4806	4.2142
		R^2	-1.8257	-2.0275	-1.9619	-1.8855	-1.7633	-1.5999	-1.4225	-1.2535
Training	Linear	RMSE	5.2967	5.9302	6.1264	6.2033	6.1787	6.0624	5.8818	5.6703
		MAE	4.2821	4.8539	4.9820	5.0092	4.9391	4.7727	4.5383	4.2713
		R^2	-1.7817	-2.0309	-1.9525	-1.8691	-1.7526	-1.6012	-1.4342	-1.2712
	Polynomial	RMSE	0.9698	0.7981	0.8325	0.8109	0.7800	0.8850	0.9109	0.8821
		MAE	0.7195	0.6049	0.6223	0.6265	0.6016	0.6786	0.6957	0.6847
		R^2	0.9067	0.9451	0.9455	0.9510	0.9561	0.9446	0.9416	0.9450
	RBF	RMSE	0.0333	0.2315	0.1039	0.4314	0.3995	0.3123	0.2316	0.1623
		MAE	0.0183	0.1548	0.0602	0.3035	0.2726	0.2113	0.1520	0.1017
		R^2	0.9999	0.9954	0.9992	0.9861	0.9885	0.9931	0.9962	0.9981
	Laplacian	RMSE	0.0000	0.0000	0.0000	0.0000	0.0000	0.0000	0.0000	0.0000
		MAE	0.0000	0.0000	0.0000	0.0000	0.0000	0.0000	0.0000	0.0000
		R^2	1.0000	1.0000	1.0000	1.0000	1.0000	1.0000	1.0000	1.0000
	Sigmoid	RMSE	1.6486	0.7634	1.6019	1.0965	1.1632	0.9449	0.7869	2.0626
		MAE	1.2481	0.5958	1.2083	0.8516	0.8922	0.7384	0.6158	1.6549
		R^2	0.7305	0.9498	0.7981	0.9104	0.9024	0.9368	0.9564	0.6995
	Cosine	RMSE	5.2979	5.9310	6.1279	6.2054	6.1808	6.0647	5.8841	5.6725
		MAE	4.2842	4.8553	4.9839	5.0095	4.9333	4.7599	4.5186	4.2461
		R^2	-1.7830	-2.0316	-1.9539	-1.8711	-1.7545	-1.6031	-1.4362	-1.2730

TABLE XI: Learning performance metrics for the models trained with the hyperparameters listed in Table IV for \mathcal{O}_{Sum} . The metrics are calculated based on the predictions made by the models on the training and testing sets for \mathcal{H}_3 with labels determined by \mathcal{O}_{Sum} . The best values for each qubit number and each metric are in bold text for the training and testing datasets. All values in this table are plotted in Figure 11, though not all of them are visible within the chosen plot range.

7. Results for \mathcal{O}_{XZ} and \mathcal{H}_4

Dataset	Kernel	Metric	Number of qubits (n)							
			5	10	15	20	25	30	35	40
Testing	Linear	RMSE	0.8851	0.9240	0.9337	0.9401	0.9424	0.9408	0.9360	0.9293
		MAE	0.8375	0.8844	0.8976	0.9061	0.9084	0.9053	0.8982	0.8878
		R^2	-5.4877	-9.7666	-12.2134	-13.2260	-13.3083	-12.7522	-11.8802	-10.6947
	Polynomial	RMSE	0.1892	0.1754	0.1597	0.1425	0.1385	0.1373	0.1195	0.1270
		MAE	0.1060	0.0914	0.0822	0.0782	0.0745	0.0814	0.0690	0.0742
		R^2	0.7034	0.6119	0.6135	0.6729	0.6911	0.7070	0.7900	0.7817
	RBF	RMSE	0.1407	0.1499	0.1218	0.1033	0.1232	0.1083	0.0950	0.0888
		MAE	0.0724	0.0731	0.0522	0.0498	0.0650	0.0577	0.0507	0.0468
		R^2	0.8360	0.7167	0.7751	0.8281	0.7555	0.8177	0.8674	0.8931
	Laplacian	RMSE	0.0974	0.1049	0.1282	0.1187	0.1159	0.1094	0.1003	0.0934
		MAE	0.0514	0.0521	0.0715	0.0686	0.0658	0.0623	0.0575	0.0536
		R^2	0.9214	0.8612	0.7511	0.7732	0.7835	0.8140	0.8521	0.8817
	Sigmoid	RMSE	0.1908	0.1774	0.1569	0.1764	0.1635	0.5520	0.2105	29.3142
		MAE	0.0981	0.0940	0.0815	0.1014	0.1055	0.3001	0.1254	17.0978
		R^2	0.6985	0.6030	0.6269	0.4990	0.5695	-3.7352	0.3487	-11636.6066
	Cosine	RMSE	0.8851	0.9218	0.9336	0.9391	0.9407	0.9384	0.9332	0.9261
		MAE	0.8376	0.8821	0.8973	0.9050	0.9068	0.9033	0.8959	0.8851
		R^2	-5.4872	-9.7161	-12.2097	-13.1944	-13.2552	-12.6843	-11.8028	-10.6139
Training	Linear	RMSE	0.8912	0.9224	0.9317	0.9352	0.9363	0.9345	0.9300	0.9233
		MAE	0.8470	0.8860	0.8965	0.9001	0.9002	0.8968	0.8903	0.8810
		R^2	-6.5416	-11.1825	-12.0591	-12.1214	-11.7599	-11.1197	-10.3358	-9.4707
	Polynomial	RMSE	0.1576	0.1181	0.1125	0.1046	0.1113	0.1131	0.0909	0.0955
		MAE	0.0884	0.0656	0.0616	0.0616	0.0641	0.0704	0.0514	0.0555
		R^2	0.7641	0.8003	0.8095	0.8358	0.8196	0.8226	0.8916	0.8879
	RBF	RMSE	0.0812	0.0831	0.0444	0.0221	0.0914	0.0796	0.0652	0.0521
		MAE	0.0434	0.0440	0.0226	0.0103	0.0510	0.0429	0.0349	0.0275
		R^2	0.9374	0.9012	0.9703	0.9927	0.8783	0.9120	0.9443	0.9666
	Laplacian	RMSE	0.0000	0.0000	0.0076	0.0048	0.0034	0.0026	0.0019	0.0002
		MAE	0.0000	0.0000	0.0051	0.0032	0.0022	0.0016	0.0012	0.0001
		R^2	1.0000	1.0000	0.9991	0.9996	0.9998	0.9999	1.0000	1.0000
	Sigmoid	RMSE	0.1130	0.1185	0.0985	0.1668	0.1557	0.6193	0.2038	32.9478
		MAE	0.0658	0.0673	0.0550	0.0976	0.0989	0.3556	0.1172	20.1928
		R^2	0.8788	0.7988	0.8540	0.5826	0.6472	-4.3227	0.4554	-13333.5415
	Cosine	RMSE	0.8922	0.9237	0.9325	0.9363	0.9374	0.9357	0.9311	0.9243
		MAE	0.8483	0.8874	0.8969	0.9003	0.9003	0.8967	0.8896	0.8797
		R^2	-6.5589	-11.2173	-12.0804	-12.1504	-11.7911	-11.1499	-10.3634	-9.4954

TABLE XII: Learning performance metrics for the models trained with the hyperparameters listed in Table V for \mathcal{O}_{XZ} . The metrics are calculated based on the predictions made by the models on the training and testing sets for \mathcal{H}_4 with labels determined by \mathcal{O}_{XZ} . The best values for each qubit number and each metric are in bold text for the training and testing datasets. All values in this table are plotted in Figure 12, though not all of them are visible within the chosen plot range.

8. Results for \mathcal{O}_{Sum} and \mathcal{H}_4

Dataset	Kernel	Metric	Number of qubits (n)							
			5	10	15	20	25	30	35	40
Testing	Linear	RMSE	7.8717	8.2751	8.3789	8.4404	8.4590	8.4367	8.3851	8.3171
		MAE	7.3590	7.8947	8.0577	8.1362	8.1498	8.1097	8.0297	7.9231
		R^2	-6.0930	-10.4791	-12.5001	-13.3118	-13.1500	-12.4112	-11.3274	-10.0421
	Polynomial	RMSE	1.1086	1.3555	1.2815	1.2502	1.4368	1.1573	1.1370	1.1639
		MAE	0.7069	0.7836	0.6983	0.7379	0.8742	0.6691	0.6764	0.7258
		R^2	0.8593	0.6920	0.6842	0.6860	0.5918	0.7476	0.7734	0.7838
	RBF	RMSE	0.8913	1.0930	0.8644	0.7940	1.0286	0.8982	0.8055	0.7614
		MAE	0.5528	0.5934	0.4079	0.3943	0.5672	0.5084	0.4461	0.4183
		R^2	0.9091	0.7997	0.8563	0.8734	0.7908	0.8480	0.8862	0.9075
	Laplacian	RMSE	0.5859	0.7574	0.9806	0.9716	0.9516	0.8828	0.8107	0.7550
		MAE	0.3555	0.4011	0.5750	0.5742	0.5497	0.5137	0.4757	0.4492
		R^2	0.9607	0.9038	0.8151	0.8103	0.8209	0.8532	0.8848	0.9090
Training	Sigmoid	RMSE	1.1541	1.3469	1.1936	1.5142	1.4086	5.2078	1.9184	223.0957
		MAE	0.7069	0.7720	0.6515	0.8967	0.9337	2.8464	1.1720	130.1390
		R^2	0.8475	0.6959	0.7261	0.5394	0.6076	-4.1101	0.3548	-7943.9105
	Cosine	RMSE	7.8679	8.2535	8.3761	8.4298	8.4419	8.4145	8.3585	8.2868
		MAE	7.3541	7.8779	8.0550	8.1268	8.1352	8.0915	8.0086	7.8983
		R^2	-6.0862	-10.4191	-12.4909	-13.2760	-13.0931	-12.3407	-11.2493	-9.9617
	Linear	RMSE	7.9094	8.2592	8.3579	8.3957	8.4016	8.3794	8.3295	8.2601
		MAE	7.4386	7.9118	8.0255	8.0652	8.0626	8.0271	7.9567	7.8595
		R^2	-6.6620	-10.8265	-11.6110	-11.5868	-11.1922	-10.5742	-9.7730	-8.8826
	Polynomial	RMSE	0.7762	0.9656	0.9374	0.9621	1.1591	0.9408	0.9154	0.9165
		MAE	0.4871	0.5608	0.5223	0.5788	0.6837	0.5476	0.5393	0.5459
		R^2	0.9262	0.8383	0.8414	0.8347	0.7679	0.8541	0.8699	0.8783
	RBF	RMSE	0.5106	0.6467	0.3556	0.1823	0.7904	0.6843	0.5594	0.4568
		MAE	0.3166	0.3636	0.1849	0.0864	0.4471	0.3794	0.3089	0.2443
		R^2	0.9681	0.9275	0.9772	0.9941	0.8921	0.9228	0.9514	0.9698
	Laplacian	RMSE	0.0000	0.0000	0.0602	0.0398	0.0281	0.0204	0.0000	0.0000
		MAE	0.0000	0.0000	0.0412	0.0266	0.0184	0.0132	0.0000	0.0000
		R^2	1.0000	1.0000	0.9993	0.9997	0.9999	0.9999	1.0000	1.0000
	Sigmoid	RMSE	0.7593	0.9347	0.8167	1.4820	1.3557	5.8739	1.8615	250.6840
		MAE	0.4922	0.5471	0.4609	0.8870	0.8745	3.3699	1.0980	153.6522
		R^2	0.9294	0.8485	0.8796	0.6078	0.6826	-4.6875	0.4620	-9101.2820
	Cosine	RMSE	7.9167	8.2705	8.3644	8.4045	8.4116	8.3895	8.3394	8.2697
		MAE	7.4446	7.9173	8.0274	8.0670	8.0634	8.0236	7.9482	7.8462
		R^2	-6.6762	-10.8590	-11.6306	-11.6133	-11.2211	-10.6022	-9.7986	-8.9055

TABLE XIII: Learning performance metrics for the models trained with the hyperparameters listed in Table V for \mathcal{O}_{Sum} . The metrics are calculated based on the predictions made by the models on the training and testing sets for \mathcal{H}_4 with labels determined by \mathcal{O}_{Sum} . The best values for each qubit number and each metric are in bold text for the training and testing datasets. All values in this table are plotted in Figure 13, though not all of them are visible within the chosen plot range.